CHAPTER 5

Effect of sidewalls on the three-dimensional wall jet

In this chapter, the effect of jet exit temperatures and the effect of sidewalls on the three-dimensional turbulent wall jet are investigated through different methods. The effect of jet temperature is investigated through the experimental method, whereas the effect of sidewalls is investigated through both experimental and numerical methods. The sidewall effect is characterised by two different wall jet configurations, i.e. configuration 1 and configuration 2. The configuration without sidewall across the jet centerline is termed as configuration 1, and the configuration with sidewall across the jet centerline is termed as configuration 2. The detailed description of the sidewall configuration is shown in chapter 3 (section 3.1.3.2). The experimental study measures the temperature and velocity field inside the flow domain with the three-dimensional transversing mechanism. The temperature field is measured with the K-type thermocouple, and an infrared thermal imaging camera measures the surface temperature. The mean velocity field is measured with a single probe hotwire anemometer. The numerical method is carried out by the two different $k-\epsilon$ low Reynolds number turbulence models, as suggested by Yang and Shih [47] (called as 'YS' hereafter) and Launder and Sharma [48] (called as 'LS' hereafter).

From the experimental and numerical methods, the effect of sidewalls is characterized by the distribution of temperature and velocity inside the flow domain, temperature and velocity decay rate of the jet centerline, the temperature decay rate of bottom wall surface, thermal spread in lateral and wall-normal directions, similarity solution. The temperature fluctuation along the axial, lateral and wall-normal directions are also investigated and presented in the form of statistical parameters. The velocity field obtained from the experimental method is presented along with numerical simulation for both the configurations. The mean velocity and temperature of the flow domain for both the configurations are used to validate the numerical results in the previous chapter 3 (section 3.2.6.2). Further, the velocity and temperature contours, maximum turbulent kinetic energy and dissipation, Skin friction coefficient, Entrainment rate, Reynolds stresses and turbulent heat flux are discussed through numerical methods.

5.1 Experimental results of with and without sidewall configurations

In the present study, the temperature and velocity profiles are presented in the non-dimensional form. The temperature (T) is normalised by jet exit central temperature (hereafter termed as jet exit temperature for simplicity) with reference to the ambient temperature and velocity is normalised by jet bulk mean velocity at the nozzle exit, as below-

$$T = \frac{t - t_o}{t_{jet} - t_o} = \frac{\triangle t}{\triangle t_{jet}} \tag{5.1}$$

Where, T is known as the normalised temperature, t is the mean temperature in ^0C, t_{jet} is the jet exit temperature in ^0C, t_o is the ambient temperature in ^0C.

5.1.1 Centerline bottom wall temperature decay

The centerline bottom wall temperature $\left(T_w = (t_w - t_o)/(t_{jet} - t_o)\right)$ is plotted for the different jet exit temperatures $\left(\triangle t_{jet} = t_{jet} - t_o\right)$ along the longitudinal direction (x/h) for a Reynolds number of $25,000$ for configurations 1 and 2 in Figure 5.1. The effect of jet exit temperatures $\left(\triangle t_{jet}\right)$ on the variation of centerline decay of the bottom wall temperature (T_w) is determined by infrared thermal imaging camera. The jet exit temperature $\left(\triangle t_{jet}\right)$ is varied from 20^0C to 40^0C above the ambient temperature. It is seen that the non-dimensional centerline surface temperature decay of the bottom wall is unaffected by the jet exit temperature for any configurations of the test setup. This can be interpreted that the effect of buoyancy is insignificant upto the jet exit temperature ($\triangle t_{jet}$), 40^0C. Xu and Antonia [55] also noticed the similar result for a free jet while Holland and Liburdy [95] claimed the buoyancy independent flow for the maximum jet exit temperature ($\triangle t_{jet}$) of 87^0C.

Further, the effect of sidewall is studied over the range of $0 \leq x/h \leq 50$. It can be seen from the Figure 5.1 that the decay of centerline surface temperature of the bottom wall is

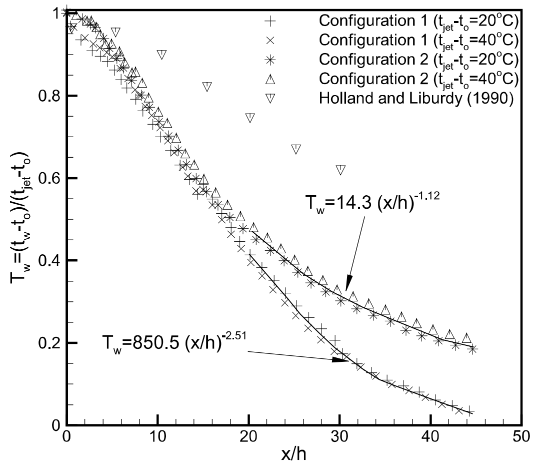

Figure 5.1: Centerline bottom wall temperature decay

unaffected in near field, before the attachment of the jet to the sidewall in configuration 2; but, after the attachment, the rate of decay of centerline temperature of the bottom wall is reduced. This is due to the sidewall, which restricts the spread of flow stream and pushes back the flow stream towards the center of the test section and simultaneously it also restricts the entrainment of ambient fluid into the flow stream, so cooling of the heated air is reduced.

The centerline surface temperature of the bottom wall of heated jet is measured by only few authors, like Holland and Liburdy [95]. Holland and Liburdy [95] measured the bottom wall temperature with the thermocouple and found similar trend as shown in Figure 5.1, but lower decay than the present case. This is due to the two dimensional flow condition considered by Holland and Liburdy [95]. The decay of surface temperature for both the configurations is described by the function as

$$T_w = A.\left(\frac{x}{h}\right)^{-B} \tag{5.2}$$

Where A and B are determined from the least square method of the experimental data. The values of A and B are found to be 850.5 and 2.51 respectively for the configuration 1 while it is 14.3 and 1.12 for configuration 2. Figure 5.1 shows the fitted profile for both the configurations. The comparison with the Holland and Liburdy [95] data indicates the influence of the three-dimensionality of the jet and the sidewall effect of the present case.

5.1.2 Lateral temperature variation of the bottom wall

The distribution of bottom wall temperature is measured with the help of thermal imaging infrared camera. The variation of bottom wall temperature profiles across the jet centerline plane ($-15 \leq x/h \leq 15$) in configuration 1 and configuration 2 are shown in Figure 5.2. Figure 5.2 indicates that the non-dimensional bottom wall temperature variation is independent of the jet exit temperature $\left(t_{jet} - t_o\right)$ for both the configurations. As the flow stream proceeds in the downstream direction, the velocity profile in the lateral direction continuously broadens across the vertical centerline plane [9, 11], due to the entrainment and mixing of the ambient fluid. This leads to a decrease in thermal energy content of the flow stream.

From Figure 5.2, it can be seen that before the attachment ($x/h < 15$) of the flow stream to the sidewalls, the bottom wall lateral temperature variation is primarily affected near the sidewall. After the attachment ($x/h > 15$) of the flow stream, the lateral spread is restricted. Due to the spread restriction, thermal energy content increases in configuration 2 than in configuration 1. The bottom wall temperature profile exhibits asymptotic nature at the edge due to the continuous decay of thermal energy in the lateral direction for configuration 1. But, this characteristics is not noticed in configuration 2 due to the presence of sidewall which restricts the lateral spread. So, after the attachment of the flow stream to the sidewall, the surface temperature is increased for configuration 2 as compared to configuration 1.

5.1.3 Centerline temperature variation

The centerline temperature $\left(T_c = (t_c - t_o)/(t_{jet} - t_o)\right)$ variation along the longitudinal direction (x/h) is measured at a distance of $0.5h$ from the bottom wall in the symmetry plane of the jet, as shown in Figure 5.3. T_c is determined with the help of K-type thermocouple mounted on a transversal mechanism. From Figure 5.3, it can be concluded that the decay of T_c is independent of the different jet exit temperatures $\left(\triangle t_{jet} = t_{jet} - t_o\right)$.

The centerline temperature variation along the flow stream is compared in Figure 5.3. It can be seen that the decay rate of the centerline temperature is reduced in configuration 2. This is due to the sidewall in configuration 2, which restricted the spread of the flow in lateral direction and thermal diffusion into the surrounding as compared to configuration 1. The decay of centerline temperature may be divided into three different regions. The first region where the temperature of the flow field is equal to the jet exit temperature ($0 \leq x/h \leq 4$), called as the potential core region. After region 1, a sharp decay of temperature occurs due to intermixing of the two shear layers, known as region 2, which occurs

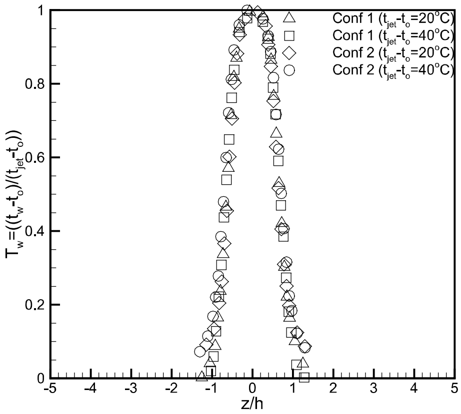

(a) $x/h = 1$

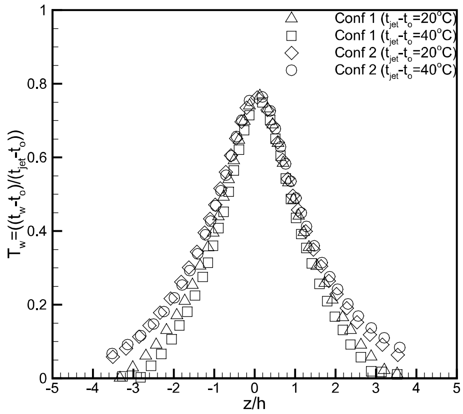

(b) $x/h = 10$

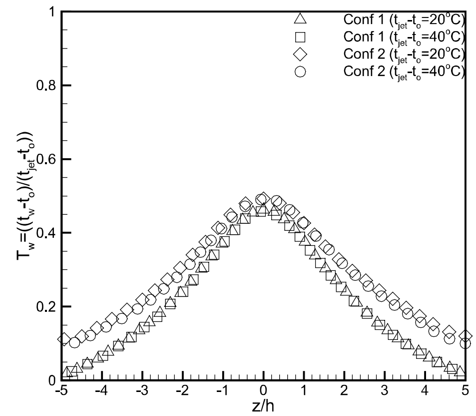

(c) $x/h = 20$

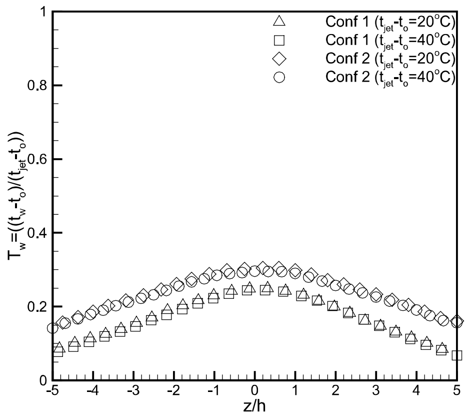

(d) $x/h = 30$

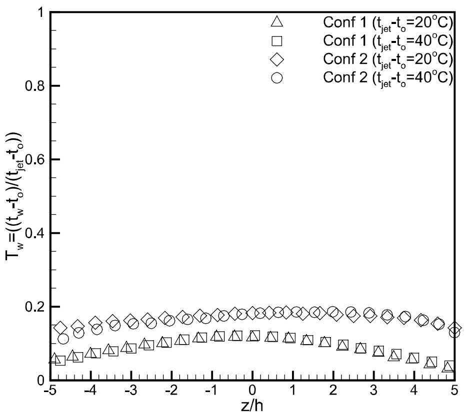

(e) $x/h = 40$

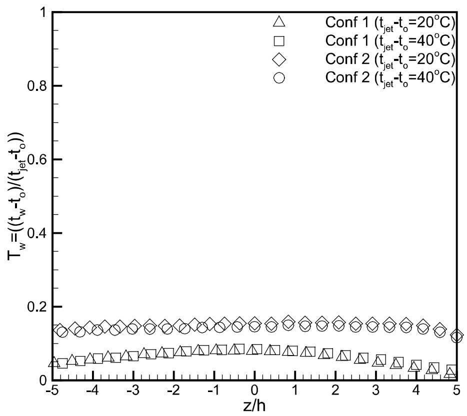

(f) $x/h = 45$

Figure 5.2: Lateral surface temperature variation in configuration 1 and configuration 2, Conf 1 = Configuration 1, Conf 2 = Configuration 2

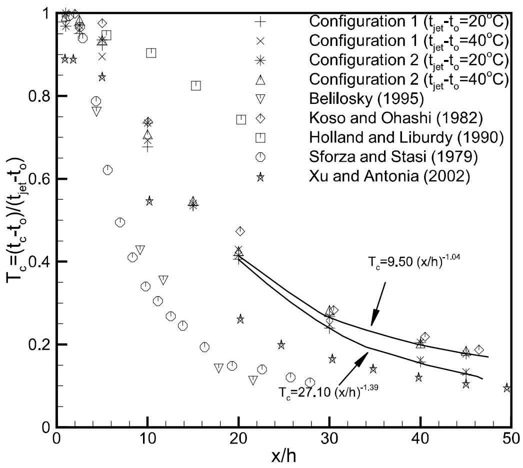

Figure 5.3: Centerline temperature decay for configuration 1 and configuration 2

between ($4 \leq x/h \leq 20$). And, the third region ($20 \leq x/h \leq 50$), where the temperature decay of the flow stream varies as per the power law according to the longitudinal distance from the jet exit,

$$T_c = A.\left(\frac{x}{h}\right)^{-B} \tag{5.3}$$

Where, the values of A and B are determined by the least square method. B is known as the decay rate of the centerline temperature in the downstream direction. The decay rate is independent of the different t_j and it is found as 1.39 and 1.04 for configuration 1 and configuration 2 respectively with $R^2 = 0.99$. The temperature decay profile along the downstream direction is compared with the results of different authors to understand the effect of the different initial and boundary conditions of the heated jet. Belilosky [97] and Koso and Ohashi [7] considered the three-dimensional heated turbulent wall jet. Belilosky [97] obtained a higher decay rate than the present case due to different jet exit velocity profiles without sidewall enclosure. From the Figure 5.3, it can be seen that the decay of mean temperature is higher than [7]. This may be due to the shape of the nozzle and bottom wall condition. Also, the mixing and entrainment of the ambient fluid in flow stream for the circular nozzle have a lower rate as compared to the non-circular case. Holland and Liburdy [19] considered the two dimensional nozzle, which resulted in a lower temperature decay rate than the present case. The temperature decay data of Sfroza and Stasi [18] and Xu and Antonia [20] are also included for the comparison of centerline temperature decay.

They considered the free jet; so the interaction area of the flow stream with the ambient fluid is higher. As a result, the rate of entrainment is higher as compared to the wall jet for configuration 1 and configuration 2.

5.1.4 Temperature distribution in the lateral ($y/h = 0.5$) and wall-normal ($z/h = 0.0$) directions

The non-dimensional lateral (y/h = 0.5) and wall-normal (z/h = 0.0) temperature distributions at various locations ($1 \le x/h \le 50$) are shown in Figures 5.4 and 5.5, respectively.

Like the bottom wall, non-dimensional lateral and wall-normal temperature distributions are independent of the jet exit temperature ($t_{jet} - t_o$). Here, only 40^0C jet exit temperature profiles are shown for brevity at the different downstream locations (x/h). Figure 5.4 shows the temperature variation in the lateral direction, measured at y/h = 0.5 for configuration 1 and configuration 2. In the radially outward direction from the jet centerline, the streamwise velocity continuously decreases due to the spreading and entrainment of the ambient fluid [9, 11], which leads to diffusion of the thermal energy into the surroundings. Due to the spreading and diffusion of thermal energy, the lateral temperature profiles broaden, similar to the velocity profiles. A similar trend is also shown by [7, 18] for the three-dimensional turbulent jet for a semi-circular nozzle. Figure 5.4 also compares temperature variation in the lateral direction for configuration 1 and configuration 2. Before attachment of the flow stream to the sidewall ($x/h \le 15$), the temperature decay shows a similar pattern near the centerline for both the configurations. A little enhancement of temperature can be seen at the edge in configuration 2 due to the formation of a weak temperature circulation zone. However, after the attachment of the flow stream ($x/h > 15$) in configuration 2, the temperature inside the test section increases, resulting in the reduction of temperature decay. Like the bottom wall temperature profile, the lateral temperature profile across the jet centerline also exhibits asymptotic nature for both the configurations upto some distance ($x/h \le 30$). Unlike configuration 1, the asymptotic nature of the temperature profile in the lateral direction is lost in the downstream locations ($x/h > 30$) for configuration 2 and it shows nearly uniform lateral temperature, as shown in Figure 5.4d. It indicates that high energy content fluid remains close to the bottom wall.

The wall-normal temperature profile for configuration 1 and configuration 2 is plotted in Figure 5.5. Before the attachment of the flow stream to the sidewalls, the wall-normal temperature profiles show less effect of the sidewall. But, after the attachment ($x/h > 15$) of the flow stream to the sidewalls, the maximum temperature difference is observed near the bottom wall between configuration 1 and configuration 2. This is due to the decrease

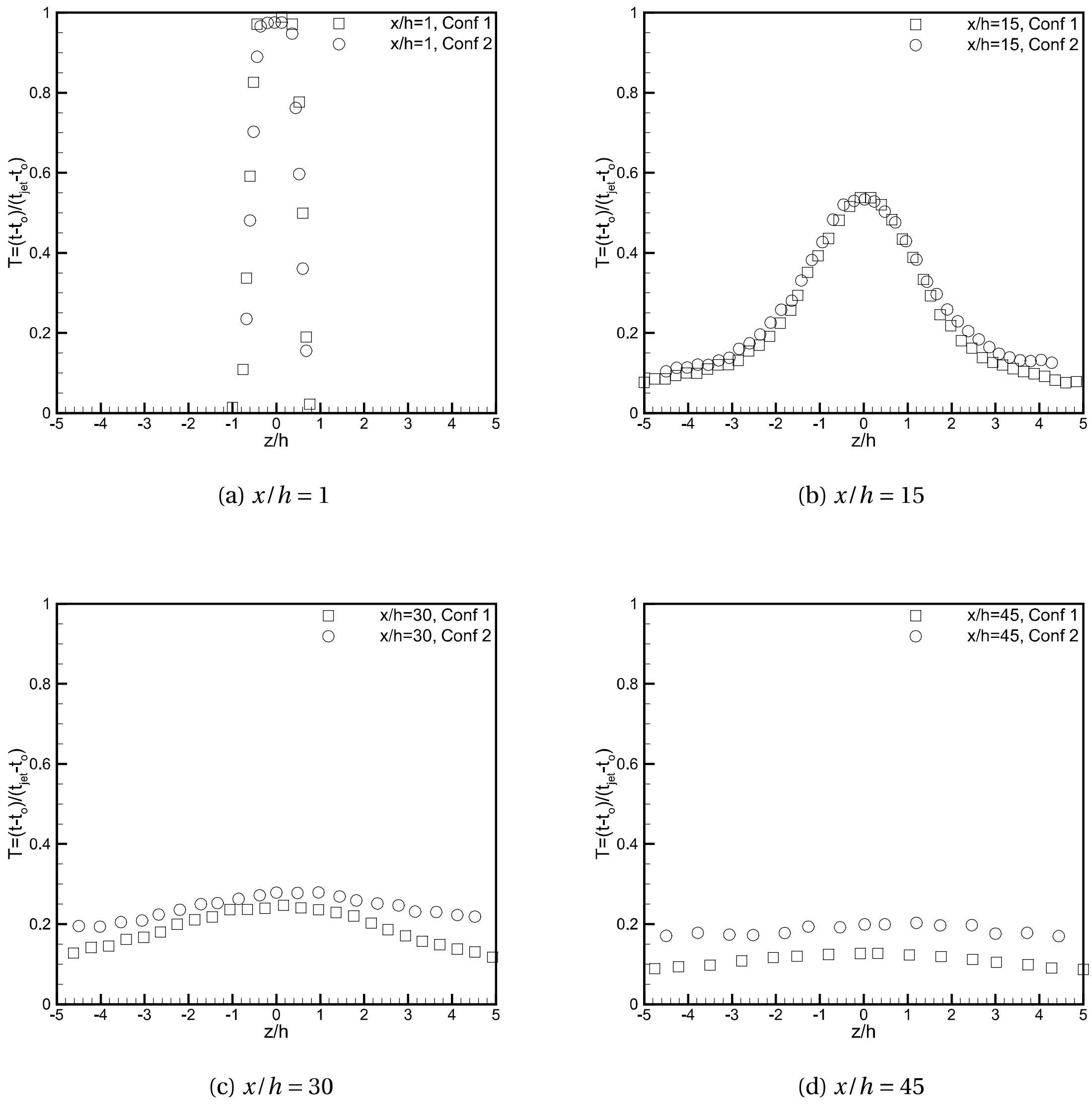

(a) $x/h = 1$

(b) $x/h = 15$

(c) $x/h = 30$

(d) $x/h = 45$

Figure 5.4: Lateral temperature variation in configuration 1 and configuration 2, Conf 1 = Configuration 1, Conf 2 = Configuration 2

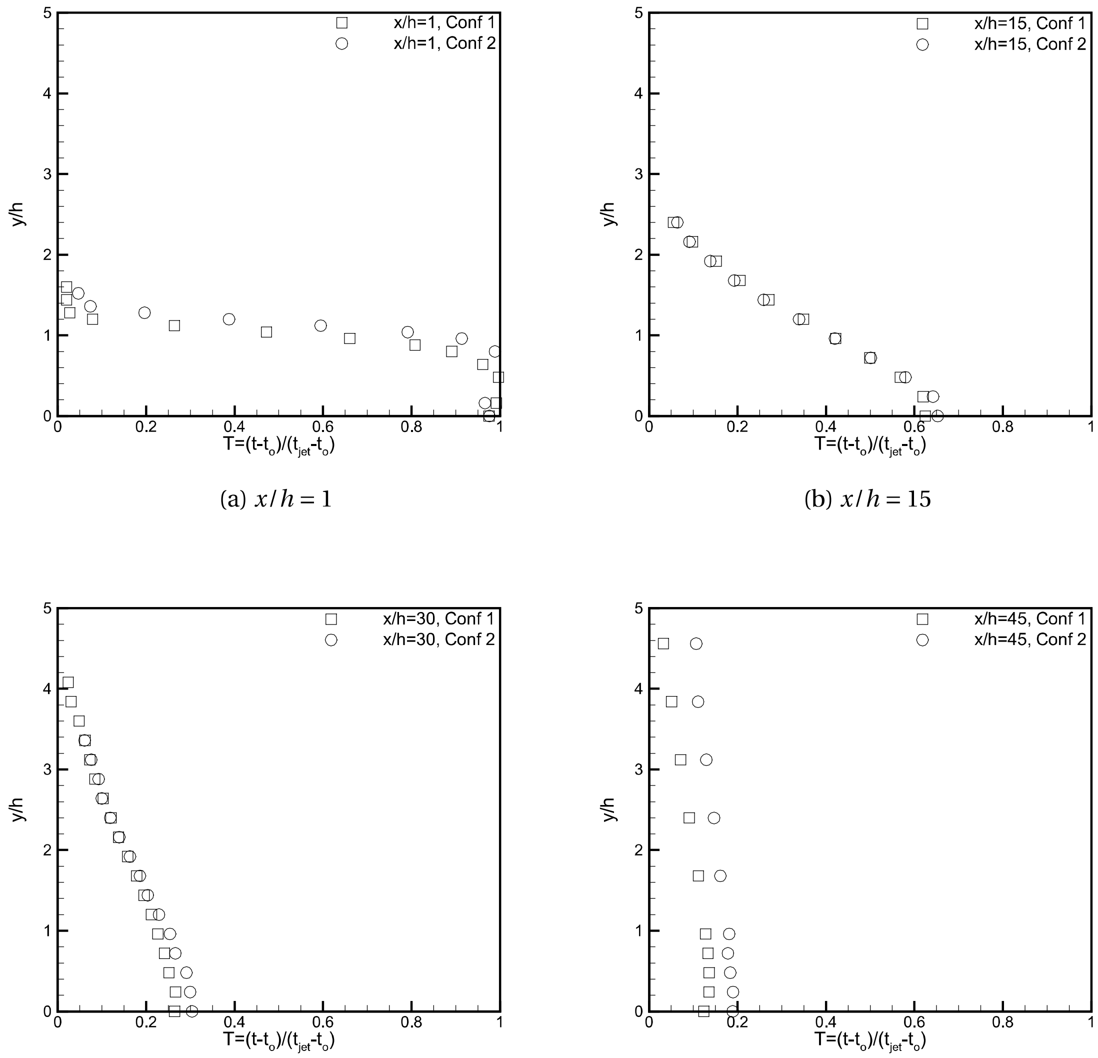

(a) $x/h = 1$

(b) $x/h = 15$

(c) $x/h = 30$

(d) $x/h = 45$

Figure 5.5: Normal temperature variation in configuration 1 and configuration 2, Conf 1 = Configuration 1, Conf 2 = Configuration 2

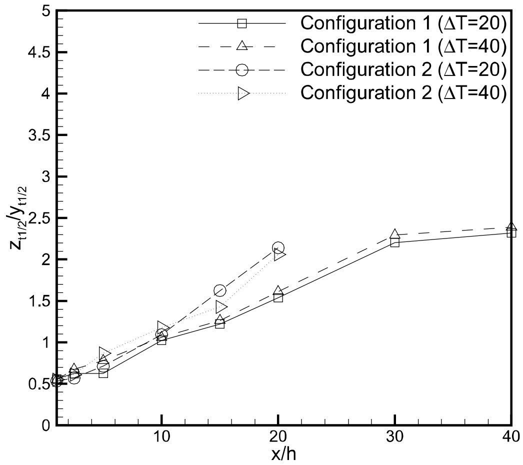

Figure 5.6: Lateral to normal thermal width ratio

in the entrainment from the surrounding fluid owing to the presence of sidewall in configuration 2. Therefore, the energy content of the fluid is higher in configuration 2 as compared to configuration 1.

Figure 5.6 shows the ratio of the lateral to wall-normal thermal half-widths. It signifies thermal spread in the lateral direction as compared to the wall-normal direction. During the design of any duct flow, like internal turbine blade and passage cooling, the half-width ratio gives the information of relative temperature spread over the flow domain. The Figure shows that the thermal width ratio increases just after the consumption of the potential core region ($x/h < 5$). After $x/h = 2.5$, the width ratio in configuration 2 is higher than in configuration 1. This signifies that the overall thermal spread of the flow stream is affected by the sidewall right from the beginning. The difference in the width ratio between configuration 1 and configuration 2 at the downstream location $x/h = 20$ is approximately 35±5 %. The variation of width ratio is nearly saturated after $x/h = 30$ in configuration 1. The width ratio in configuration 2 can not be evaluated after $x/h > 20$ due to the uniform temperature across the jet centerline.

5.1.5 Thermal half-width

The spreading and diffusion of the fluid energy into the surrounding are determined with the thermal half-width. The thermal half-width $(y_{t1/2}, z_{t1/2})$ is defined as the location of the temperature, where $t = t_m/2$; t_m is the maximum mean temperature at that location.

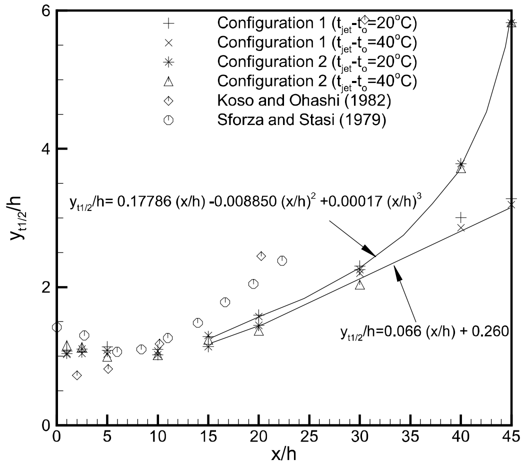

Figure 5.7: Thermal half-width ($y_{t1/2}/h$ Vs x/h) in wall-normal direction for configurations 1 and 2 $\left(\triangle t_{jet} = 20°C, 40°C\right)$ and compared with Koso and Ohashi [7] and Sforza and Stasi [18]

Thermal half-width shows how far the jet temperature penetrates in the wall-normal and lateral directions.

Figure 5.7 shows the downstream variation of the non-dimensional thermal half-width in the wall-normal direction. Figure 5.7 shows the variation of thermal half-width for the different jet exit temperatures $\left(\triangle t_{jet} = t_{jet} - t_o\right)$. It is noticed that the thermal half-width is unaffected by the jet exit temperature. The thermal half-width linearly varies with the downstream distance (x/h) for configuration 1, while it is nonlinear for configuration 2. It is noticed that the thermal half-width is also unaffected by the sidewall before the attachment of the flow to the sidewall ($x/h < 15$). But after the attachment, $y_{t1/2}$ increases non-linearly for configuration 2. This is because the dissipation of energy is restricted in configuration 2 owing to the presence of sidewall while the energy continuously dissipates in configuration 1. A comparison has been made for the thermal half-width with Koso and Ohashi [7] and Sforza and Stasi [18] . From Figure 5.7, it can be seen that all the jets exhibit similar behaviour with a little alteration for configuration 1. This may be due to the shape of the nozzle, surrounding condition, the rate of diffusion of the ambient fluid into the flow stream, type of wall and the jet arrangement. A linear equation is fitted for configuration 1 and a nonlinear third order polynomial equation is fitted for configuration 2 for $y_{t1/2}$ as,

$$\frac{y_{t1/2}}{h} = a\left(\frac{x}{h}\right) + b \tag{5.4}$$

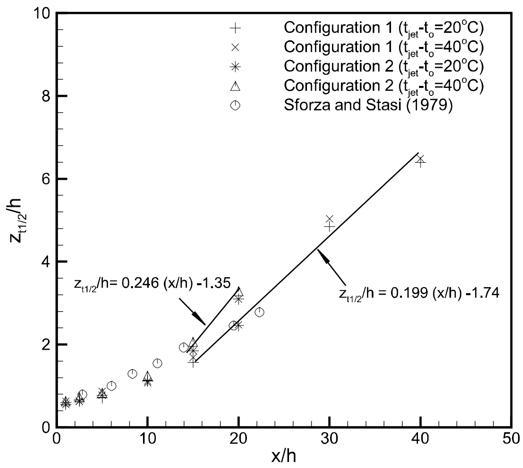

Figure 5.8: Thermal half-width ($z_{\mathrm{t}1/2}/h$ Vs x/h) in lateral direction for configuration 1 and 2 $\left(\triangle t_{jet} = 20°C, 40°C\right)$ and compared with Sforza and Stasi [18]

$$\frac{y_{\mathrm{t}1/2}}{h} = a\left(\frac{x}{h}\right) + b\left(\frac{x}{h}\right)^2 + c\left(\frac{x}{h}\right)^3 \tag{5.5}$$

The value of constant is calculated for the range $15 \le x/h \le 45$ with the least square method for both the configurations, as shown in the Figure, with a goodness of fit about 98%.

Figure 5.8 shows the variation of thermal half-width in the lateral direction for configuration 1 and configuration 2. The thermal half-width is calculated for different $\triangle t_j$ for both the configurations. Similar to the wall-normal direction, $z_{t1/2}$ remains same for both the configurations till $x/h = 15$. Thereafter, $z_{t1/2}$is little suppressed in configuration 1 as compared to configuration 2 because of more dissipation of energy to the entrained fluid. The spread of the jet half-width is compared with Sforza and Stasi [18] and a similar trend is noticed. A linear equation is also fitted for the lateral direction as:

$$\frac{z_{\mathrm{t}1/2}}{h} = a\left(\frac{x}{h}\right) + b \tag{5.6}$$

The values of a, b are 0.199, -1.74 and 0.246, -1.35, for configuration 1 and configuration 2 respectively. The goodness of fit $\left(\mathrm{R}^2\right)$ is about 98% for both the configurations.

5.1.6 Similarity profile

The thermal similarity profiles for configuration 1 and configuration 2 are calculated for the different locations in the physical coordinate of $(t - t_o)/(t_m - t_o)$ with $z/z_{t1/2}$ and $y/y_{t1/2}$

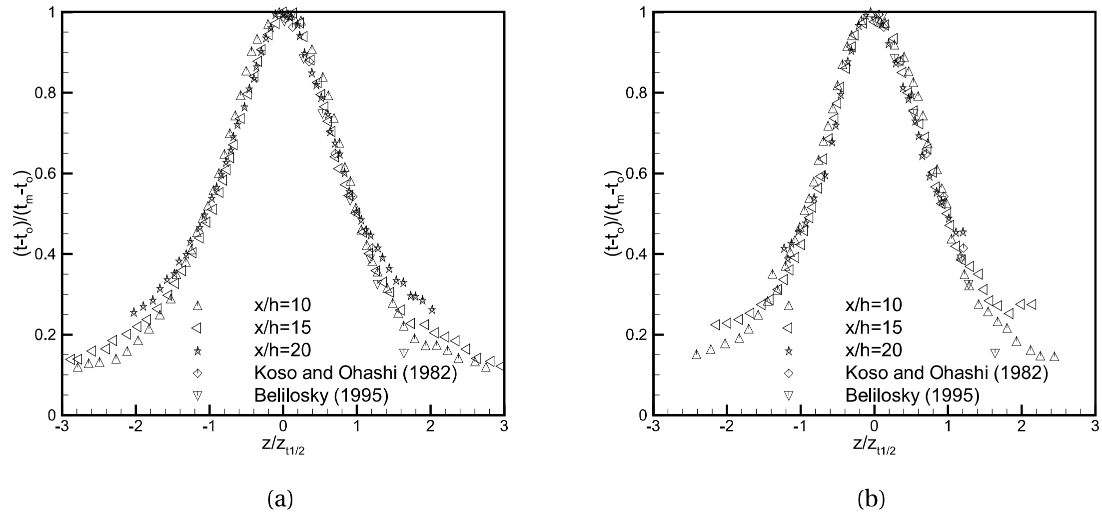

Figure 5.9: Self-similarity in lateral direction (a) Configuration 1 (b) Configuration 2

in the lateral (Figure 5.9) and wall-normal (Figure 5.10) directions respectively. The lateral similarity is measured on a plane located at a distance of $0.5h$ from the bottom wall while normal similarity is measured in wall-normal symmetry plane. The self similarity profile in the wall-normal and lateral directions is found independent of the jet exit temperature ($\triangle t_{jet}$).

From Figure 5.9, it is noted that the temperature profiles attain self-similarity in the lateral plane at x/h=15 and 10 in configuration 1 and configuration 2 respectively, indicating higher turbulence structures present in configuration 1 as compared to configuration 2 due to the interaction between ambient fluid and the flow stream, which is suppressed in configuration 2 due to the sidewall. The similarity profile for the temperature of Koso and Ohashi [7] and Belilovsky [97] is also included for the comparison purpose as shown in Figure 5.9. The Figure shows a good agreement with the published results.

The temperature similarity profiles for configuration 1 and configuration 2 in normal plane at different locations are shown in Figure 5.10. From the Figure, it can be noticed that unlike lateral plane, the self-similarity profile for both the configurations is unaffected by the presence of sidewall and it is achieved at $x/h = 15$. This is quite obvious as the temperature profile in the wall-normal direction will be influenced more by the lower wall than the sidewalls.

Figure 5.10 also shows the comparison of similarity profile in the wall-normal direction for the different types of nozzle geometry and wall and jet configurations. The other authors have adopted different forms of normalization to get the self similarity profile. For

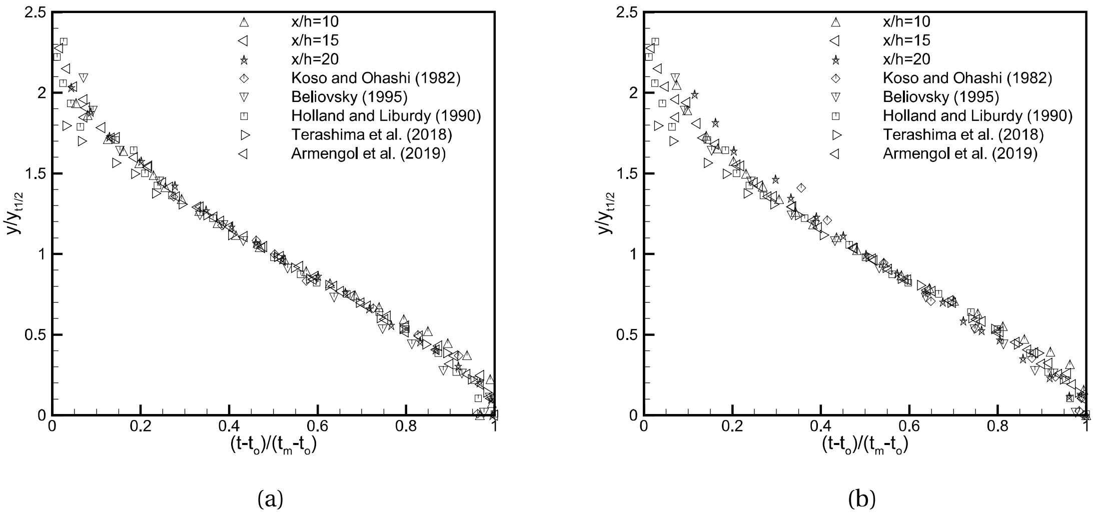

Figure 5.10: Self-similarity in wall-normal direction (a) Configuration 1 (b) Configuration 2

the wall jet case the abscissa has been normalized by the maximum temperature at that location while for the free jet, it is normalized by the centerline temperature. Koso and Ohashi [7] got the thermally self similar profile for three dimensional wall jet at $x/h = 20$ in wall-normal and lateral direction for a semicircular nozzle while Belilovsky [97] reported the self similarity at $x/h = 4.2$. The similarity profile in wall-normal plane of the two dimensional wall and free jet (Holland and Liburdy [95], Terashima et al. [141] and Armengol et al. [142]) are also included for the comparison and it shows quite good agreement in thermally developed region.

5.1.7 Thermal turbulent structure

Mean characteristics of a turbulent jet exhibit only some part of the flow information. So, the measurement of the turbulent flow structure becomes important to define the diffusion and entrainment of the ambient fluid into the flow stream in three dimensional turbulent wall jet. The heated turbulent flow structure depends on the different characteristics of the turbulent jet like velocity and temperature fluctuation in different directions and entrainment of the ambient fluid into the flow stream. In the heated jet, there are only few literature [7, 20, 77, 90, 92] available on two and three dimensional turbulent jet, where they have studied the temperature fluctuations. Here, the effect of sidewall on temperature fluctuation in configuration 1 and configuration 2 is studied. The fluctuating temperature of the flow field in configuration 1 and configuration 2 is presented in non-dimensional form. The effect of sidewall is also discussed in terms of fluctuating temperature and entrainment of the ambient fluid.

5.1.7.1 Temperature fluctuation at different sections in lateral and wall-normal directions

The temperature fluctuation is drawn in the lateral and wall-normal directions at different locations (as indicated by the legends) for configuration 1 and configuration 2 in Figures 5.11 and 5.12 respectively. Figures 5.11a and 5.11b show the fluctuation in the lateral and wall-normal directions respectively for the configuration 1. It is interesting to observe the different trends shown by the two directions. In the lateral direction, it is noticed that the minimum fluctuation is observed near the jet centerline, where the production of fluctuation is diminished when $x/h = 5$. At this location, the fluctuation starts increasing in radially outward direction due to the diffusion and intermixing with the ambient fluid. The maximum fluctuation is observed near the interface of the flow stream and the stagnant air. While, in the wall-normal direction, the fluctuation is more or less constant at $x/h = 5$ indicating that the side infiltration is more dominant than the top infiltration. The fluctuation becomes more or less constant at $x/h = 20$ in both the directions. But, the fluctuation increases drastically after $x/h = 20$, resulting in the more turbulence even near the centerline. Figures 5.12a and 5.12b show the fluctuation in the lateral and wall-normal directions respectively for configuration 2. It shows the similar trend as configuration 1 near the maximum mean velocity of the flow stream at $x/h = 5$ in the lateral direction. One interesting feature can be seen in Figure 5.12a at $z/h = 3$, where the fluctuation attains a maximum value. The reason behind this is quite obvious because the jet attaches to the sidewall near $x/h = 15$ in configuration 2. But, the overall fluctuation in configuration 2 is reduced as compared to configuration 1 due to the less interaction with the ambient fluid. Koso and Ohashi [7] reported the higher fluctuation with the similar trend in the wall-normal and lateral directions for configuration 1. This may be due to the shape of the nozzle and the bottom wall boundary conditions. Antonia et al. [88] also reported the minimum rms fluctuations $\left(< (t - t_{mean})^2 >^{1/2}\right)$ in lateral direction near the local maximum mean velocity. They also mentioned that in radially outward direction, fluctuation increased due to the intermixing with the ambient fluid. Antonia et al. [88] also noticed the higher fluctuation than the present case due to the more interaction area with the ambient fluid.

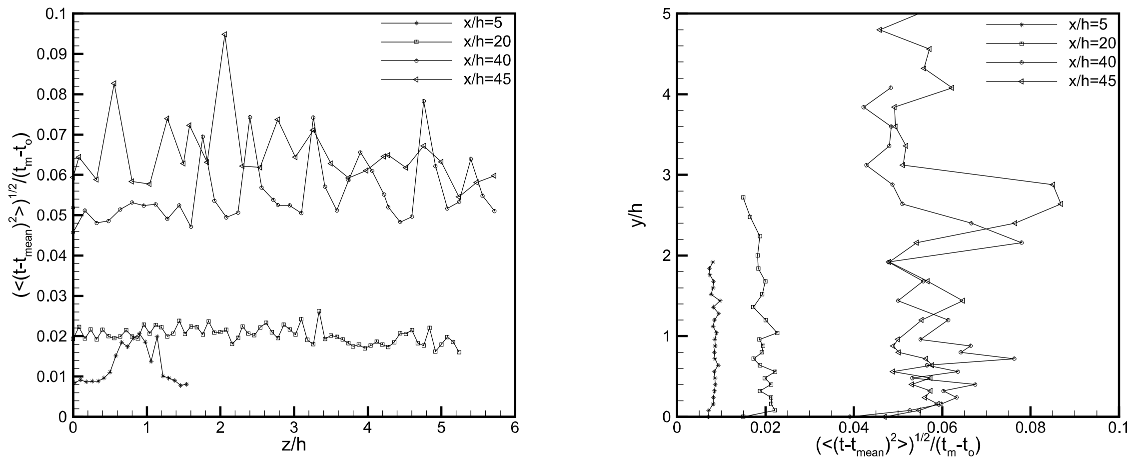

(a) (b)

Figure 5.11: Temperature fluctuation for configuration 1 in (a) Lateral direction (b) Normal direction

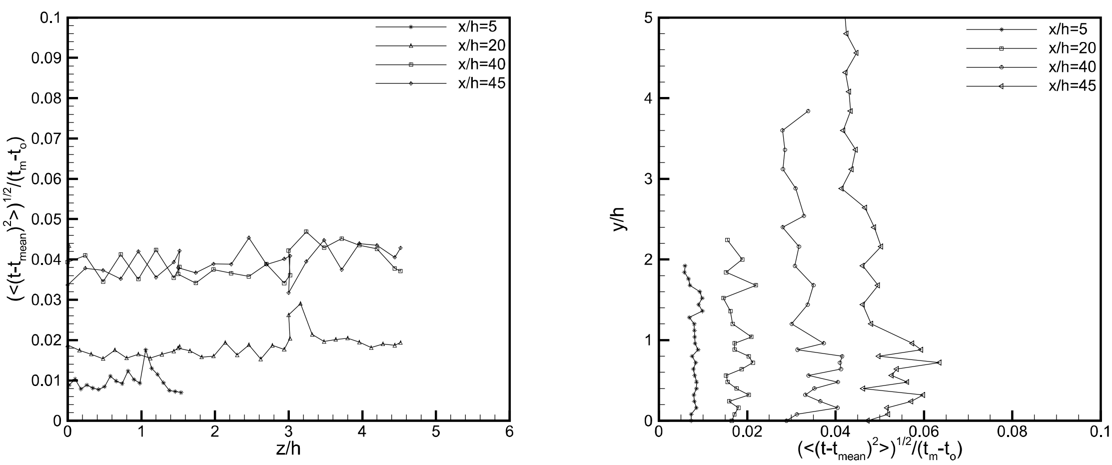

(a) (b)

Figure 5.12: Temperature fluctuation for configuration 2 in (a) Lateral direction (b) Normal direction

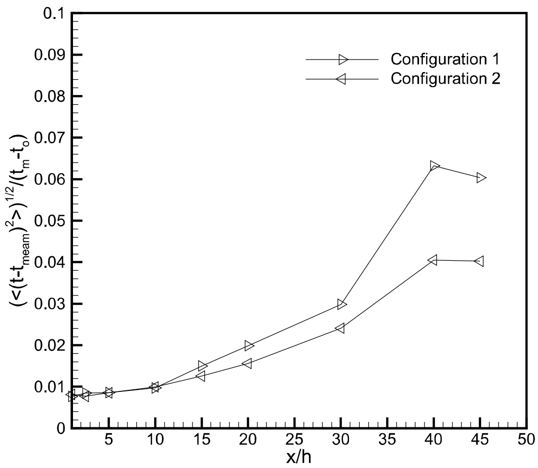

Figure 5.13: Centerline temperature fluctuation for configuration 1 and configuration 2

5.1.7.2 Temperature fluctuation along the center line

The rms temperature fluctuation $\left(< (t - t_{mean})^2 >^{1/2}\right)$ along the centerline is shown in Figure 5.13 for configuration 1 and configuration 2. From the Figure, it can be concluded that as the flow stream leaves the nozzle a lower fluctuation is observed due to the potential core. This potential core extends upto $x/h = 5$ in the downstream direction. The rms temperature fluctuation intensity $\left(< (t - t_{mean})^2 >^{1/2} / (t_m - t_o)\right)$ in this region is about 0.008 for both the configurations, which indicates that the sidewall does not play any role in this region. After the consumption of the potential core, due to intermixing of the upper and lower shear layers and the entrainment of the ambient fluid, a sudden increase of temperature fluctuation is observed. Therefore, a sharper decay in temperature is observed in this region as shown in the temperature decay profile for both the configurations (Figure 5.3). This result supports the trend observed by Zhang and Chua [143] and Xu and Antonia [20]. The fluctuation intensity in the present case is lower than the reported in different literature due to the different boundary conditions and nozzle geometry. The highest fluctuation is observed in between $30 \leq x/h \leq 45$. In this range, the fluctuation is higher for configuration 1 as compared to configuration 2. This is due to the higher entrainment of the ambient fluid in configuration 1 as compared to configuration 2.

5.1.8 Probability density function of temperature fluctuations

The probability density functions (PDF) of the one-point fluctuating temperature (θ) at different locations are calculated at the jet centerline ($y/h = 0.5$) lateral plane. The one point fluctuating temperature is normalised by its own r.m.s. $\left(\theta' = (<(t - t_{mean})^2>^{1/2})\right)$. It is seen that the one point normalised fluctuating temperature follows the normal distribution. The distribution of the PDF is normalised such that $\Delta_0^\infty \mathrm{P}\big(\theta/\theta'\big)\mathrm{d}\big(\theta/\theta'\big)$=1. The normal distribution curve is shown along with the experimental one point fluctuating temperature distribution data.

The PDF of centerline (y/h = 0.5, z/h = 0.0) for configuration 1 and configuration 2 is shown in Figure 5.14. From the Figure, it can be seen that the PDF in the near field (x/h < 15) is deviated from the normal curve due to the jet interaction with the ambient fluid. In configuration 2, due to the presence of the sidewalls, the temperature of the ambient fluid is more than in configuration 1. This results in the scattered probability of the fluctuating temperature inside the flow domain about the mean fluctuating probability; but in configuration 1, due to the lower temperature of the ambient fluid, the probability of the temperature fluctuation is concentrated near the mean fluctuating probability. This is due to the different ambient fluid conditions and the lower mixing in near field. As the flow develops in the downstream direction (x/h > 15), it spreads in the lateral and wall-normal directions and starts mixing with the ambient fluid. Therefore, interaction with the surrounding cold fluid is also increased resulting in an increase in the range of fluctuating temperature for both the configurations [91]. It is also evident that due to the presence of sidewall, the interaction of the cold fluid with the flow stream is restricted in configuration 2 as compared to configuration 1. So, the fluctuating range of instantaneous temperature exhibits a narrow band in configuration 2 with respect to the configuration 1. This fact can be seen in Figure 5.14, which shows the PDF at different locations along the centerline. At the downstream locations x/h = 15, 20, and 40, where the flow stream interacts with the sidewall in configuration 2, a rapid diffusion of the thermal energy content occurs between the shear layers leading to the deviation of PDF curve from the normal distribution curve. While in configuration 1, due to the entrainment of the cold ambient fluid inside the flow stream, the range of fluctuating temperature increases; but due to the cold ambient fluid, the probability of the fluctuating temperature increases near the mean probability point. For configuration 2, due to the presence of the sidewall, the dominance of large scale vortex structure would be there, which resulted in uniform mixing of the fluid. On the other hand, the sidewall restricts the entrainment from the side, resulting in a lower fluctuating temperature range and has maximum probability near the mean temperature.

The shape of the probability density function (PDF) curve represents the degree of the small scale mixing [144]. For distinguishing the extreme range of fluctuating temperature between configuration 1 and configuration 2 at the different lateral locations (on the

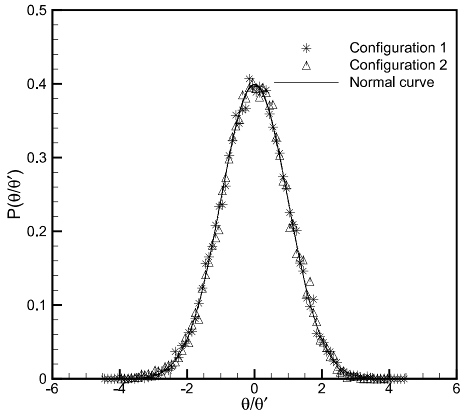

(a) $x/h = 5$

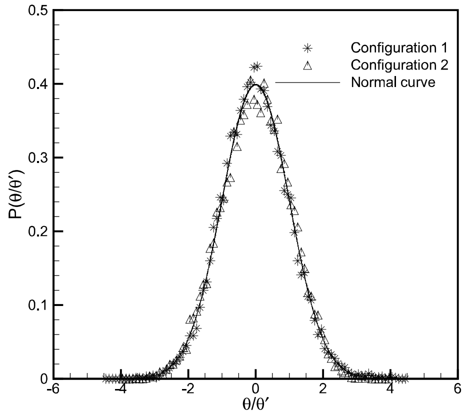

(b) $x/h = 10$

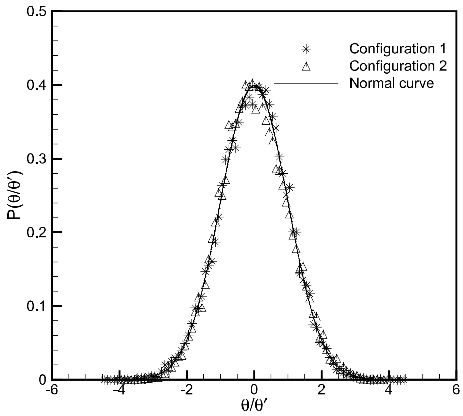

(c) $x/h = 15$

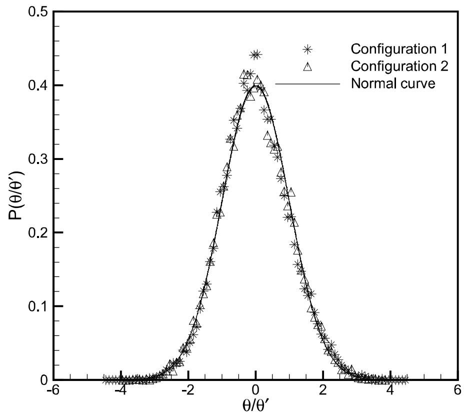

(d) $x/h = 20$

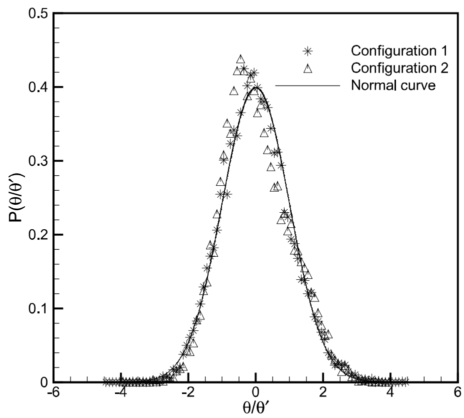

(e) $x/h = 40$

Figure 5.14: Centerline probability density function (PDF) for configuration 1 and configuration 2

$y/h = 0.5$ plane), the probability density function is presented on a logarithmic scale, i.e. $\log(\theta/\theta')$ vs (θ/θ'). For this, three distinct lateral locations ($x/h = 10$, 20, and 40) are chosen corresponding to the fluctuating temperature for configuration 1 and configuration 2 to include the effect of sidewall and entrainment of the ambient fluid. At, $x/h = 10$, the jet stream only interacts with the ambient fluid (Figure 5.15). The PDF curve follows the normal distribution curve in both the configurations but the range of the temperature fluctuation is higher in configuration 1 than in configuration 2 in the lateral plane ($y/h = 0.5$) at $x/h = 10$, indicating higher mixing of the ambient fluid in configuration 1 than in configuration 2 in the lateral direction. Further, in the lateral location of $z/h = -1$ (Figure 5.15b), at the downstream location $x/h = 10$, a higher deviation is observed from the normal distribution curve. This is due to the interaction between the flow stream and the ambient fluid. This suggests that the range of the temperature fluctuation is more in configuration 1 than in configuration 2. Further, as the jet develops in the downstream locations, the jet stream starts interacting with the sidewalls and the ambient fluid. As, mentioned earlier, due to the presence of sidewall, the range of fluctuating temperature is reduced in configuration 2; so is the case in the lateral direction. After the interaction of the flow stream with the sidewall ($x/h = 20$) in configuration 2, the distribution of PDF is compared in Figure 5.16. These Figures suggest that the probability distribution of fluctuating temperature is deviated from the normal distribution curve for configuration 2 due to the mixing of the flow stream in configuration 2. Also, it shows a lower range of single point temperature fluctuation. While in configuration 1, it follows the normal probability distribution curve and the range of fluctuating temperature is enhanced. In the downstream location ($x/h > 40$), the turbulent fluctuation structure tends to get stabilised near the wall and again the distribution of PDF follows a normal distribution in both the configurations, as shown in Figure 5.17. Some of the authors have calculated the probability density function for the free jet (Cesar Dopazo [145], Lockwood and Moneib [90], Mi et al. [144], Mi et al. [91], Pietri et al. [146], Xu and Antonia [20]). It is interesting to note here that all of them have observed the normal distribution of the one-point fluctuating temperature. The interaction of ambient fluid in the case of free jet is higher than any of the bounded jet, so the PDF of fluctuating temperature range is higher than the present case.

5.1.9 Skewness and Flatness of fluctuating temperature

The centerline ($y/h = 0.5$, $z/h = 0.0$) skewness factor $\left(S_\theta = <\theta^3> / <\theta^2>^{3/2}\right)$ and flatness factor $\left(F_\theta = <\theta^4> / <\theta^2>^2\right)$ for configuration 1 and configuration 2 are calculated for the one-point fluctuating temperature. The type of PDF is the representation of the skewness and flatness factors. Altogether 13,000 data points of the temperature fluctuation θ are

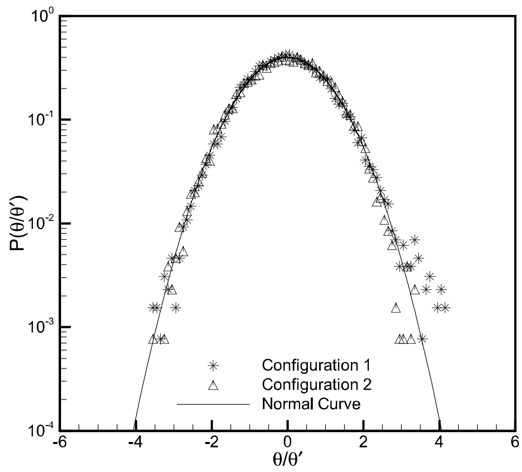

(a) $z/h = 0$

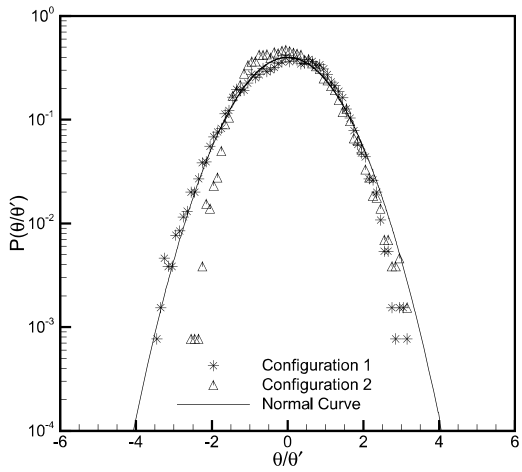

(b) $z/h = -1$

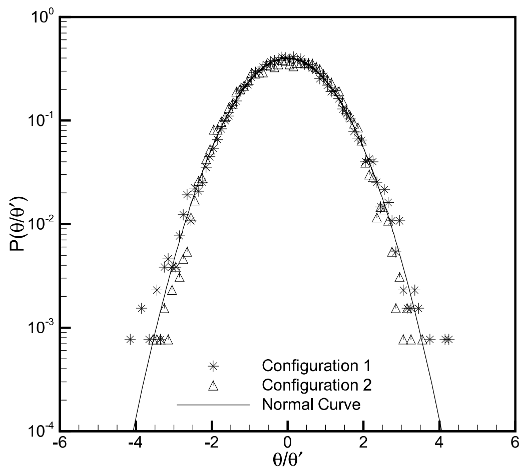

(c) $z/h = -2$

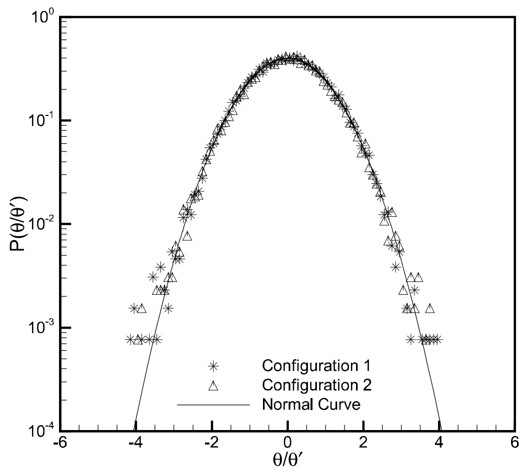

(d) $z/h = -3$

Figure 5.15: Probability density function (PDF) for configuration 1 and configuration 2 at $x/h = 10$

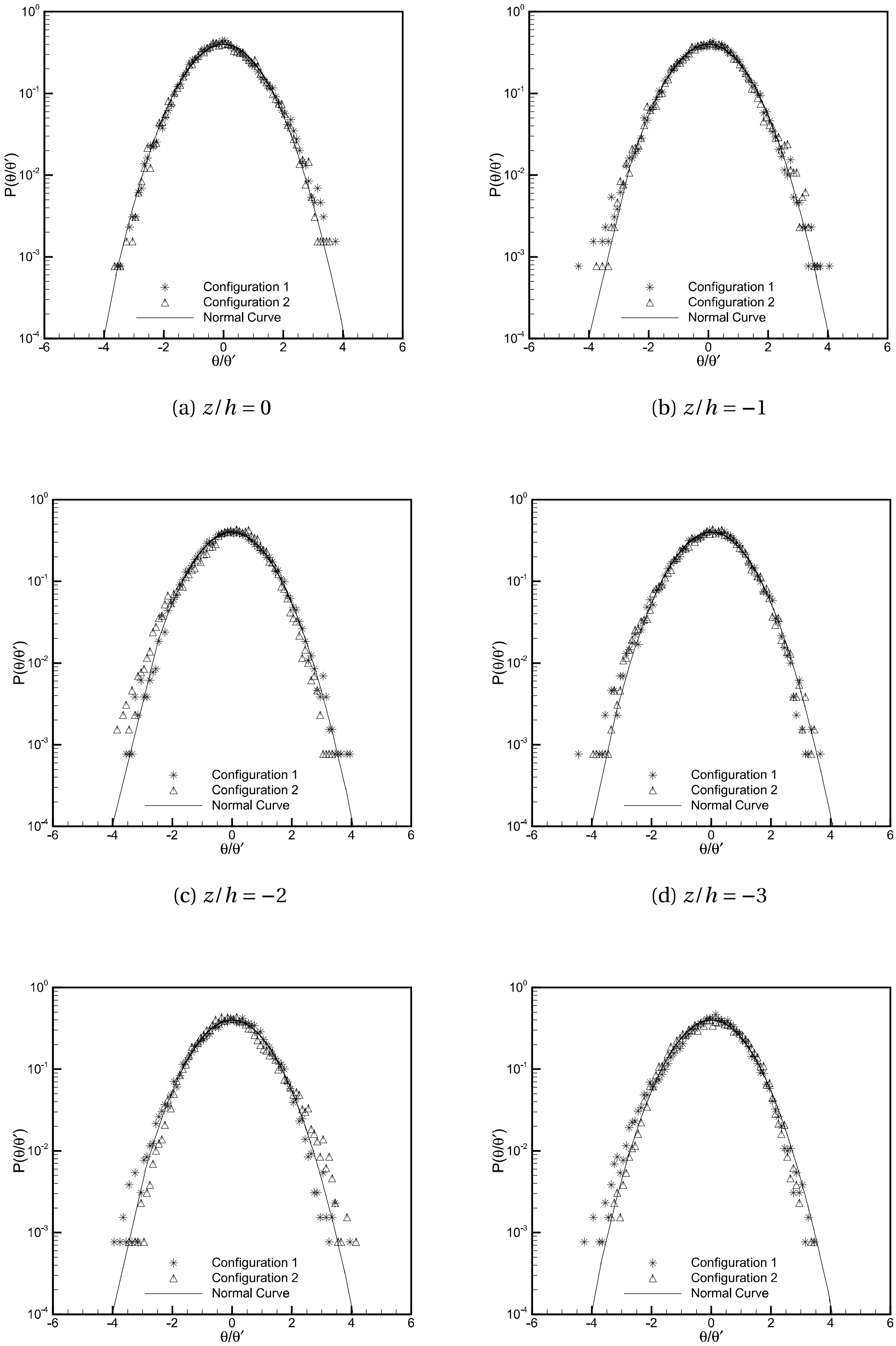

(a) $z/h = 0$ (b) $z/h = -1$

(c) $z/h = -2$ (d) $z/h = -3$

(e) $z/h = -4$ (f) $z/h = -4.5$

Figure 5.16: Probability density function (PDF) for configuration 1 and configuration 2 at $x/h = 20$

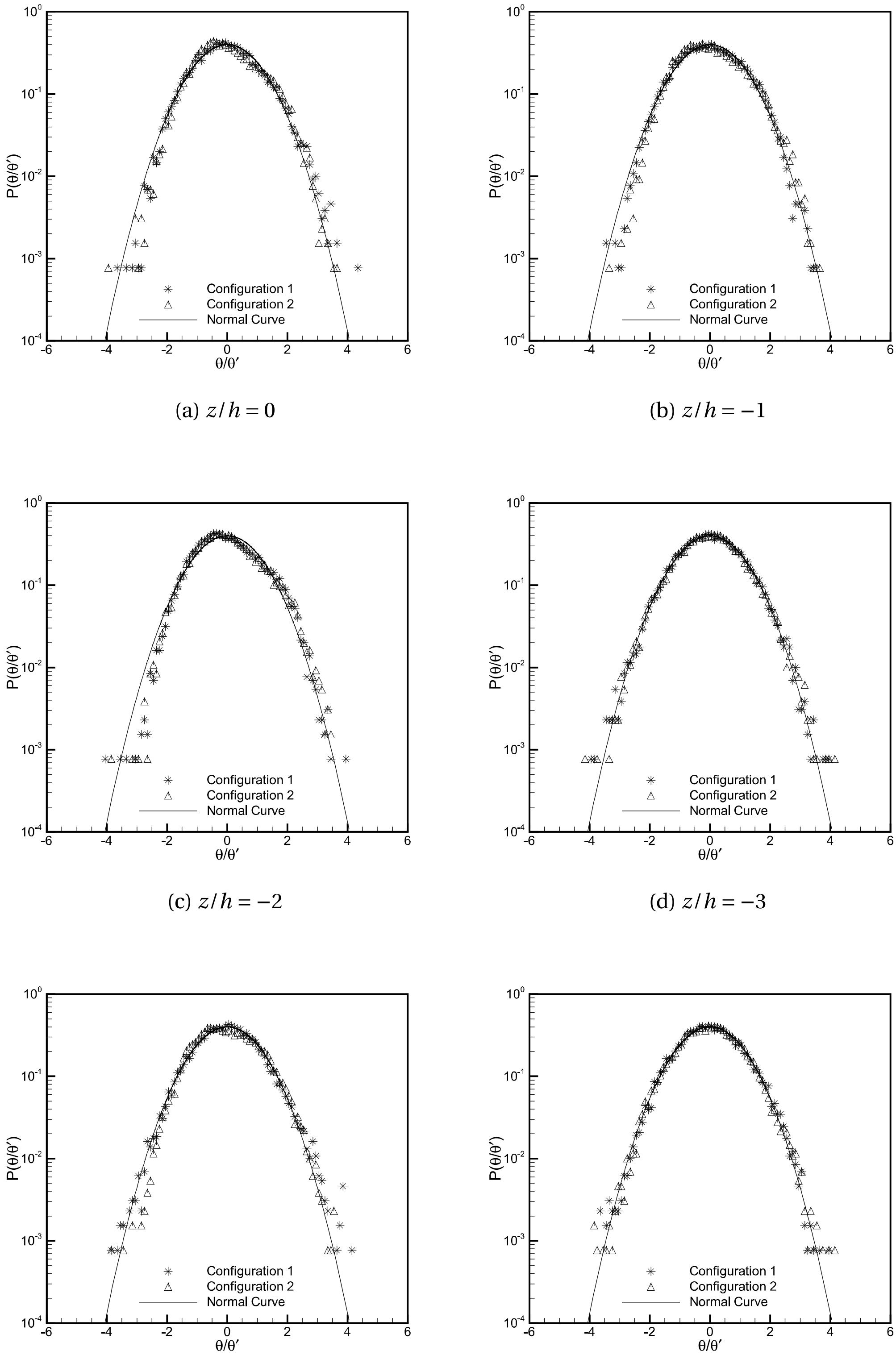

(a) $z/h = 0$

(b) $z/h = -1$

(c) $z/h = -2$

(d) $z/h = -3$

(e) $z/h = -4$

(f) $z/h = -4.5$

Figure 5.17: Probability density function (PDF) for configuration 1 and configuration 2 at $x/h = 40$

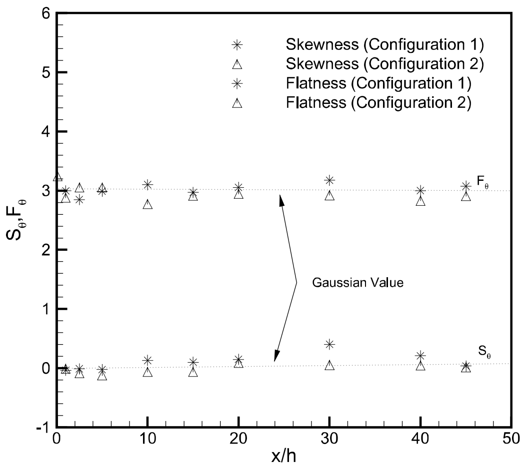

Figure 5.18: Skewness and Flatness about centerline

considered to calculate the skewness and flatness factors along the jet centerline. These skewness and flatness factors data are consistent with the PDF of the fluctuating temperature distribution for configuration 1 and configuration 2. These factors behave differently for configuration 1 and configuration 2 because of the influence of surrounding entrainment and sidewall condition. The negative skewness represents the strong dominance of the convection from the hot flow stream [90]. The evaluation of skewness and flatness along the jet centerline is shown in Figure 5.18. From the Figure, negative skewness is dominated in near field of the jet for both the configurations due to the potential core. This negative skewness stays longer in configuration 2 as compared to configuration 1, which reflects the domination of hot packets in jet fluids in configuration 2. The positive value of skewness and flatness factors is due to the mass entrainment from the surrounding cold fluid into the hot flow stream, which remains higher for configuration 1 in far-field location as compared to configuration 2. The value of skewness and flatness is higher at $x/h = 30$ for both the configurations. It indicates the presence of large scale vortex structure which allows the entrainment at a higher rate. The value of these factors remain higher for configuration 1 as compared to configuration 2 due to more interaction of surrounding cold fluid. The average value of skewness and flatness factors in far-field locations ($x/h > 20$) is (0.199, 3.075) and (0.048, 2.899) for configuration 1 and configuration 2 respectively. These values are comparable with the data obtained by Mi et al. [91] for free jet over the entire range of $x/h \geq 25$, where they got the value of skewness and flatness factors for contraction and pipe jet as (-0.36, 3.20) and (-0.28, 3.07) respectively. Similar case was also studied by Xu and Antonia [20]. They reported flatness factor slightly higher

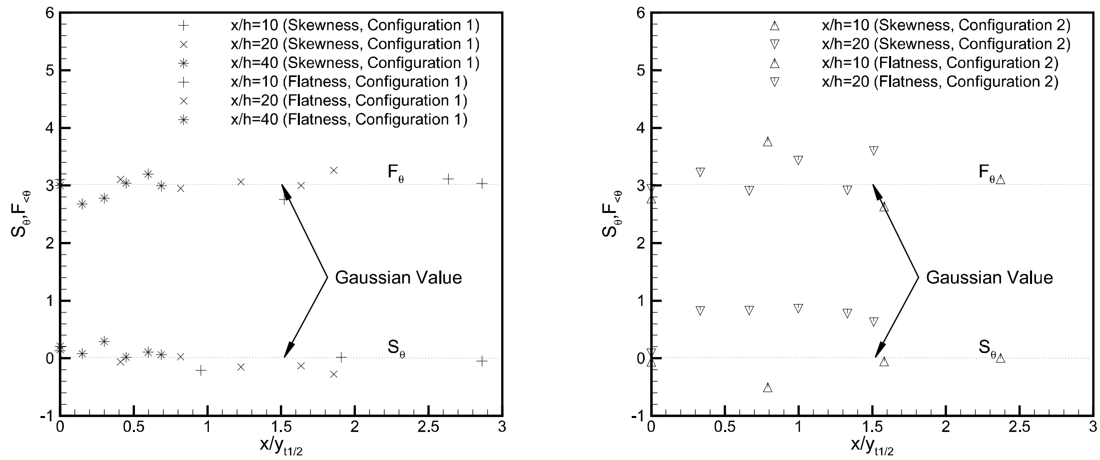

(a) (b)

Figure 5.19: Similarity behaviour (a) Configuration 1 (b) configuration 2

than the Gaussian values (=3.0) for both the jets.

Skewness and flatness factors are calculated at three different locations (x/h = 10, ,20, and 40) in the lateral direction (on the y/h = 0.5 plane) to compare configuration 1 and configuration 2. The maximum deviation of the skewness and flatness factors from the Gaussian value occurs at x/h = 20. This deviation is higher for configuration 2 as compared to configuration 1 due to the fluid and sidewall interaction. Data of skewness and flatness across the lateral direction is presented in the form of self-similarity (Figure 5.19) for both the configurations, as suggested in literature [90, 91, 144]. The Figure depicts the statistical property of the PDF of the three-dimensional turbulent jet. It shows that self-similarity is achieved earlier in configuration 1 as compared to configuration 2. This is due to the fluid and wall interaction in configuration 2, that leads to large vortex in the flow stream.

5.2 Numerical results of with and without sidewall configurations

The velocity and heat transfer characteristics in both the configurations are presented in the form of non-dimensional quantities. The velocity and temperature are non-dimensionalised as:

$$T = \frac{t - t_o}{t_{jet} - t_o} \tag{5.7}$$

and

$$U = \frac{u}{u_{jet}} \tag{5.8}$$

where, t is the temperature inside the flow field, t_{jet} is the temperature of the flow stream at the nozzle exit, t_o is the ambient temperature, u is the streamwise mean velocity and u_{jet} is the jet exit velocity. In the code validation section it is noticed that the YS model nearly predicts 6% more accurate result as compared to LS model for a heated three dimensional wall jet. In the results and discussion section, the variation of the temperature and velocity flow field, Reynolds shear stress and turbulent heat flux are shown only for YS model for the brevity, whereas for other phenomena, the result from YS and LS models are shown.

5.2.1 Centerline temperature and maximum velocity decay

The decay of centerline temperature $\left(T_c = (t_c\text{-}t_o)/(t_{jet}\text{-}t_o)\right)$ and maximum streamwise velocity (U_{max}=u_{max}/u_{jet}) decay along the downstream direction are shown in Figure 5.20. In this Figure, the decay of temperature and velocity is plotted from a virtual origin x_o as suggested by Wygnanski et al. [32]. The streamwise distance is measured from the virtual origin x_o, where any fitted line to the data converge to u_{max}/u_{jet}=1 at $x = x_o$. The decay of centerline temperature and maximum velocity along the downstream direction are predicted by the low Reynolds number YS and LS turbulence models. The data of Kumar and Kumar [147] are used for comparison of the centerline temperature decay in both the configurations. The maximum velocity decay along the downstream direction is measured with the single probe hotwire anemometer and compared with the numerical results. From the Figure 5.20, it can be seen that the sidewall affects the temperature decay just after the potential core region whereas the velocity decay is affected in the fully developed region. This is due to the different rates of heat loss occurring just after the potential core region with the surrounding in configuration 1 and configuration 2. In configuration 1, higher diffusion of thermal energy occurs whereas sidewalls restrict the diffusion of thermal energy in configuration 2 after a certain location. The velocity variation is observed after the attachment of the flow stream to the sidewalls. The presence of sidewalls restricts the entrainment and increases the turbulent viscosity in configuration 2 as compared to configuration 1. Due to this, the resistance offered to the flow stream enhances

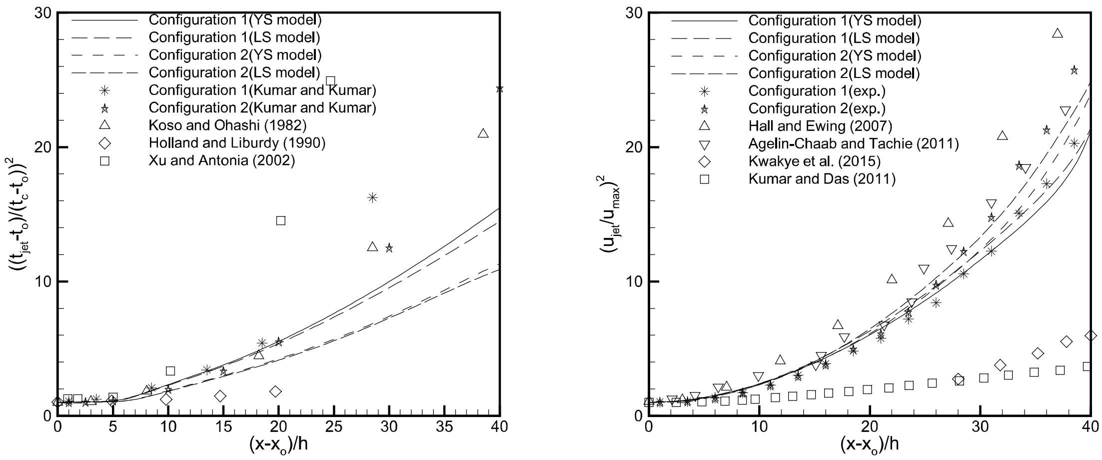

(a) (b)

Figure 5.20: Decay of (a) Centerline temperature and (b) maximum velocity along the downstream direction

in configuration 2, which results in the loss of momentum. This leads to a rapid decay of maximum streamwise velocity in configuration 2 as compared to configuration 1. The centerline temperature (T_c) and maximum streamwise velocity $\left(u_{max}/u_{jet}\right)$ in the far field locations are fitted in a traditional decay correlation curve along the downstream direction (x/h) as follows:

$$\frac{(t_c\text{-}t_o)}{(t_{jet}\text{-}t_o)} = T_c \propto \left(\frac{x}{h}\right)^{-B} \tag{5.9}$$

$$\frac{u_{max}}{u_{jet}} = U_{max} \propto \left(\frac{x}{h}\right)^{-n} \tag{5.10}$$

The constant value is determined with the help of least square method. B and n are known as the decay rates of the jet centerline temperature and the maximum velocity respectively. The decay rates of the centerline temperature and maximum velocity obtained by LS and YS turbulence models are listed in table 5.1. The numerical results suggest that the decay rate of temperature decreases in configuration 2 by nearly 25% as compared to configuration 1, whereas decay rate of velocity increases in configuration 2 by nearly 8-9% as compared to configuration 1. The decay rate predicted by the LS model is close to the experimental value for the velocity field, whereas the decay rate predicted by the YS model is close to the experimental results for the temperature field. The LS model is approximately 0.9% more accurate than the YS model for predicting the maximum velocity

Table 5.1: Decay rate of centerline temperature and maximum velocity along the downstream direction

	LS Model	YS Model	Experimental
Configuration 1	B=1.27	B=1.29	B=1.39
	n=0.98	n=0.98	n=1.04
Configuration 2	B=0.95	B=0.97	B=1.04
	n=1.07	n=1.06	n=1.07

decay rate (n), whereas YS model is approximately 2% more accurate for the temperature decay rate (B). The generation of the room draught at the downstream locations and measurement technique (intrusive in nature) may be the reason for the deviation between the numerical and experimental results. The numerical results are obtained considering the surrounding medium as quiescent, which is very hard to maintain in the experimental conditions. The LS model predicts a higher decay of the local maximum mean velocity whereas YS model predicts a higher decay of the local jet centerline temperature. This is due to the different wall damping functions used in these (YS and LS) models, which create different rate of mixing of the jet fluids.

The decay of centerline temperature and maximum velocity are compared with the results found in the literature and it is noticed that behaviour is almost similar. The three-dimensional turbulent wall jet of Koso and Ohashi [7] shows a higher temperature decay rate than the present case. This is due to the bottom wall boundary condition and different shapes of the nozzle. The shape of the nozzle permits the entrainment and mixing with the ambient fluid at different rates, which allows different decay rates. Holland and Liburdy [19] shows a lower decay of centerline temperature as compared to the present case. This is due to the two dimensional flow assumed by the authors [19]. A round free jet condition of Xu and Antonia [20] has a higher decay rate than the present case due to the higher interaction area with the surrounding. The maximum streamwise velocity is compared with the three-dimensional wall jet nozzle condition of Hall and Ewing [9], Agelin-Chaab and Tachie [11]. [9] and [11] used fully developed velocity profile while in the present case, a developing velocity profile is used. Kwakye et al. [13] and Kumar and Das [14] have a lower decay rate than the present case. [13] used a rectangular nozzle with high aspect ratio and [14] used a two dimensional nozzle.

5.2.2 Temperature and velocity contour

The distribution of velocity and temperature in configuration 1 and configuration 2 is tested by contour plots through LS and YS turbulence models. The normalised velocity components (u/u_{jet}, v/u_{jet} and w/u_{jet}) and temperature ($T = (t-t_o)/(t_{jet}-t_o)$) are plotted at two different downstream locations ($x/h = 5$ and 25) as shown in Figures 5.21 and 5.22. The negative value in the contour plot shows the entrainment inside the flow domain, whereas the positive value shows the spreading behaviour of the flow-field. At the downstream location $x/h = 5$, it can be seen from Figure 5.21 that the distribution of streamwise mean velocity component $\left(u/u_{jet}\right)$ inside the lower shear layer is nearly similar in both the configurations but in the upper shear layer, a little higher spread is observed in configuration 1 as compared to configuration 2. This is due to the enhancement in the generation of turbulent kinetic energy in configuration 2 as compared to configuration 1, which leads to an increase in the momentum loss in the upper shear layer in configuration 2. The distribution of v and w velocity components also starts showing the effect of sidewalls very near to the jet exit. It is noticed from the contours of v and w that the strength of velocity in configuration 1 is higher than in configuration 2. This leads to a higher entrainment inside the shear layers in configuration 1. The higher spread of streamwise velocity component $\left(u/u_{jet}\right)$ in configuration 1 leads to a higher spread of temperature in upper shear layers, but higher entrainment inside the shear layers leads to more loss of thermal energy in configuration 1 as compared to configuration 2. Therefore, the maximum temperature in configuration 1 is decreased with increase in the spread of the temperature field.

At the downstream location $x/h = 25$ (Figure 5.22), the sidewall starts interacting more intensely with the flowstream in configuration 2. This leads to a higher mixing inside the flow domain and consequently, higher momentum loss in configuration 2. The momentum loss in configuration 2 results in a less spread of the jet; so, the configuration 1 has higher spread of streamwise velocity as compared to configuration 2. However, the lateral and normal velocity components in configuration 2 start increasing at this location as compared to configuration 1. This characteristic of the flow enhances the entrainment inside the shear layer in configuration 2. The temperature spread in configuration 1 is also higher.

5.2.3 Generation of maximum turbulent kinetic energy and dissipation

The turbulent kinetic energy is the unique characteristic of a fluctuating flow because it indicates the strength of the turbulence within the flow field. The turbulent kinetic energy (k_n) is related to the energy contained by different size of eddies available inside the flow. The generation of turbulent kinetic energy inside the flow field is explained by Biswas [133] with the shear parameter $\left(Sh = (x/u) * \left(du/dy\right)\right)$. If shear parameter $Sh < 1$, the turbulent kinetic energy always dissipates with increase in the downstream direction but if the shear

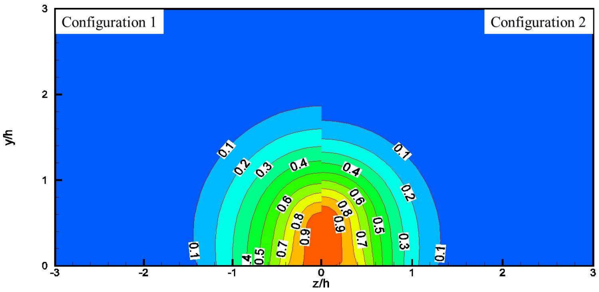

(a)

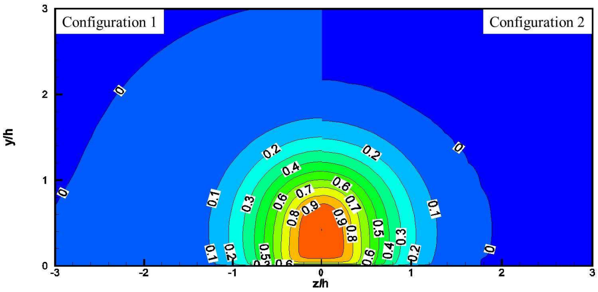

(b)

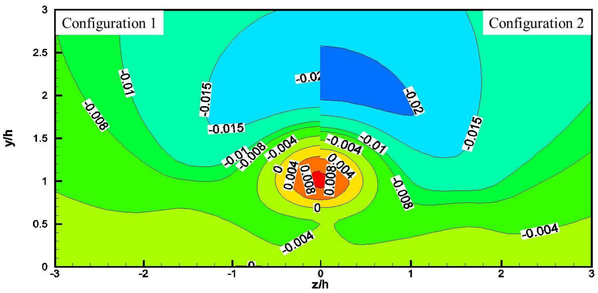

(c)

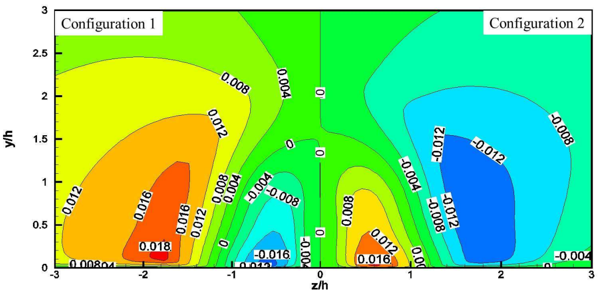

(d)

Figure 5.21: Contour plot at $x/h = 5$ for YS model (a) Temperature contour in configuration 1 and configuration 2 (b) u velocity contours in configuration 1 and configuration 2 (c) v velocity contour in configuration 1 and configuration 2 (d) w velocity contour in configuration 1 and configuration 2

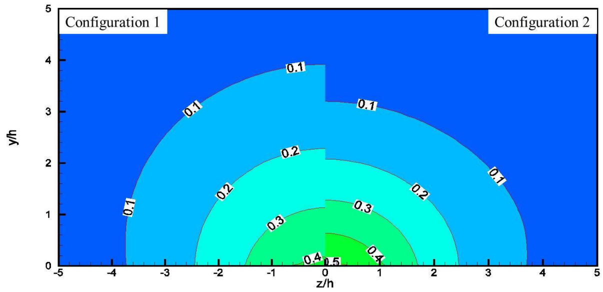

(a)

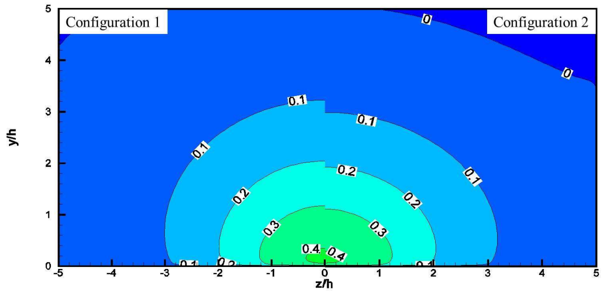

(b)

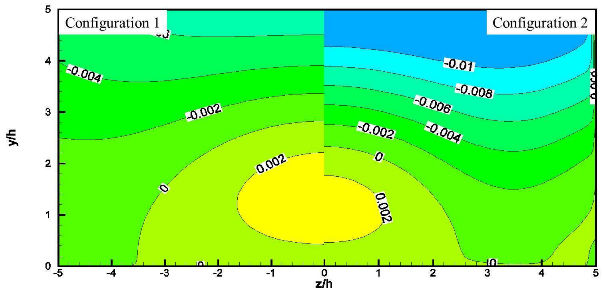

(c)

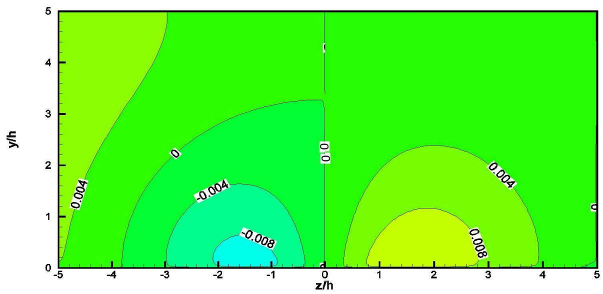

(d)

Figure 5.22: Contour plot at $x/h = 25$ for YS model (a) Temperature contour in configuration 1 and configuration 2 (b) u velocity contours in configuration 1 and configuration 2 (c) v velocity contour in configuration 1 and configuration 2 (d) w velocity contour in configuration 1 and configuration 2

parameter $1 < Sh < 3.5-4$, then flow maintains the same kinetic energy throughout the flow field. In the present case, the shear parameter is found $Sh < 1$ for both the cases. So, the strength of turbulent kinetic energy gradually decreases in the downstream locations. The effect of sidewalls inside the flow field is seen at different downstream locations in the generation of maximum turbulent kinetic energy and dissipation as shown in table 5.2. The maximum production of the turbulent kinetic energy is in the upper shear layer (at the interface of flow stream and stagnant fluid) whereas the maximum dissipation occurs in the inner shear layers (near the bottom wall). In the near field ($x/h \leq 5$), the generation of turbulent kinetic energy is dependent on the initial condition of the jet whereas in far field locations, the local disturbance of the flow domain is responsible for generation of turbulent kinetic energy. From table 5.2, it can be seen that the generation of maximum turbulent kinetic energy is initially (i.e. $x/h \leq 5$) higher in configuration 1 due to higher strength of lateral (w) and wall-normal (v) velocity components. Further downstream, the flowstream starts interacting with the sidewalls in configurations 2 which results in an increase in the maximum kinetic energy. The difference in turbulent kinetic energy gradually increases and it reaches nearly 10 at $x/h = 30$. The dissipation occurs inside the inner shear layer or boundary layer region. The dissipation of turbulence energy represents the heat and momentum transfer through turbulent diffusion. In near field, the dissipation of turbulent energy is higher in configuration 1 as compared to configuration 2 because of the entrainment, but in the downstream locations, sidewalls reversed this trend in configuration 2.

5.2.4 Skin friction coefficient

The wall shear stress for configuration 1 and configuration 2 is presented in the form of skin friction coefficient. The skin friction coefficient C_{fw} of a three-dimensional wall jet is expressed as

$$C_{fw} = \frac{\tau_{wall}}{\frac{1}{2}\rho u_{max}^2} \tag{5.11}$$

Where, τ_{wall} is the wall shear stress at the different downstream locations and ρ and u_{max} are fluid density and local maximum streamwise velocity respectively. The variation of the skin friction coefficient for both the configurations is shown in Figure 5.23. From the Figure 5.23, it can be seen that the skin friction coefficient is relatively high near the jet exit due to the presence of high velocity gradient in both the configurations. After exit from the nozzle, it starts interacting with the bottom wall. So, a sudden drop of velocity occurs which leads to a decrease in the skin friction coefficient in both the configurations.

Table 5.2: Generation of maximum turbulent kinetic energy and dissipation

x/h	k_n				ε_n			
	Configuration 1		Configuration 2		Configuration 1		Configuration 2	
	YS model	LS model	YS model	LS model	YS model	LS model	YS model	LS model
5	0.03103	0.03065	0.03080	0.03033	0.03179	0.05111	0.03081	0.05038
10	0.02722	0.02729	0.02770	0.02765	0.02731	0.04282	0.02703	0.04247
15	0.02031	0.02016	0.02093	0.02078	0.01807	0.02498	0.01857	0.02562
20	0.01364	0.01341	0.01429	0.01403	0.00829	0.01081	0.00856	0.01099
25	0.00926	0.00904	0.00988	0.00959	0.00391	0.00418	0.00402	0.00419
30	0.00643	0.00616	0.00707	0.00677	0.00196	0.00194	0.00199	0.00195

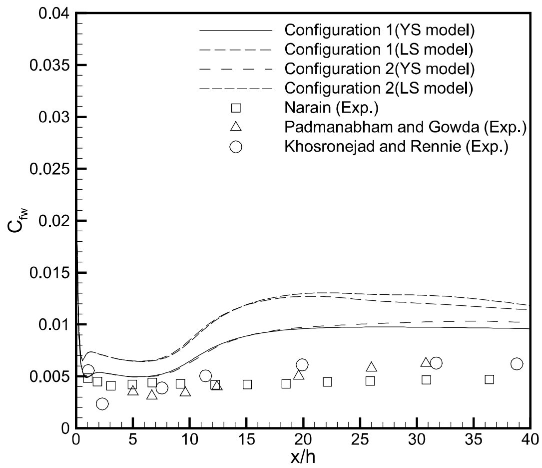

Figure 5.23: Variation of skin friction coefficient (C_{fw})

After attaining a minimum value, the skin friction coefficient again increases and reaches a local peak at a downstream location $x/h = 2$ due to the expanding nature of the jet. But, due to the presence of bottom wall, a slight depression is observed up-to $x/h = 7$. After the downstream location $x/h = 7$, the skin friction coefficient gradually increases due to the development of the three-dimensional wall jet. Eventually, the skin friction coefficient approaches a constant value in both the configurations. The skin friction coefficient nearly overlaps each other up-to the downstream location $x/h = 18$ due to similar spreading condition in both the configurations. But after the attachment of the flowstream to the sidewalls, the decay of maximum streamwise velocity increases in configuration 2. So, configuration 2 offers higher resistance as compared to configuration 1 and value of the skin friction coefficient increases in configuration 2. The present numerical results are compared with the experimental results of Narain [21], Padmanabham and Gowda [2] and Kosronejad and Rennie [22] and a similar variation of the skin friction coefficient is noticed. From the Figure, it can be seen that the skin friction profile predicted by YS model reveals less deviation as compared to LS model. The different initial and boundary conditions used by the different authors are also the reason for the deviation in the skin friction profile. The present numerical results are also compared with the coefficient value of Narain [21] and Sforza and Herbst [105] for far-field locations in table 5.3 and found in the accepted range of -0.075 to -0.22 [2, 105] reported in the literature of the experimental data. The reported value of Narain [21] falls in between the YS and LS models, whereas Sforza and Herbst [105] reported the higher value as compared to both the models.

Table 5.3: Skin friction coefficient comparison

Authors	Experimental	YS model	LS model
Narain [21]	-0.110	-	-
Sforza and Herbst [105]	-0.22	-	-
Configuration 1	-	-0.150	-0.095
Configuration 2	-	-0.170	-0.103

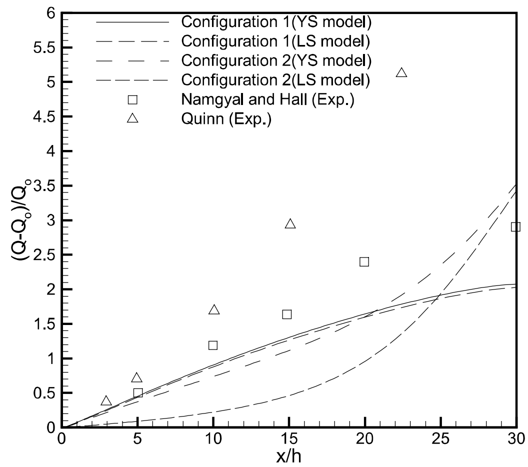

Figure 5.24: Mass entrainment ratio into the flowstream

5.2.5 Entrainment rate

The variation of the mass entrainment ratio along the downstream direction for both the configurations is shown in Figure 5.24. The mass entrainment ratio is calculated at the different downstream locations as $(Q - Q_o)/Q_o$. Where, $Q\left(= \triangle \rho \overline{u}\, dydz\right)$ is the mass flow rate at any downstream location and Q_o is the mass flow rate at the nozzle exit. Figure 5.24 shows that the entrainment ratio linearly varies along the downstream location. Both the models show similar variation of the mass entrainment, but LS model shows a little less value as compared to the YS model. This is due to the different damping coefficients used in these two models. The entrainment ratio in configuration 1 is higher as compared to configuration 2 up-to the downstream location x/h = 20.7 (YS model) and x/h =24.6 (LS model). This is due to the generation of high strength of crosswise and normal velocity components in configuration 1. But, after the downstream location x/h = 20.7 (YS model) and x/h = 24.6 (LS model), the entrainment in configuration 2 is enhanced. This characteristic of the jet is obtained due to the sidewalls, which significantly enhances the Reynolds shear stress inside the flow domain leading to an increase in the mixing characteristics of the jet. The present numerical result is compared with the free jet exiting from the sharp edged round nozzle of Quinn [148] and a three-dimensional wall jet generated by a contoured round nozzle of Namgyal and Hall [23]. The entrainment ratio is nearly two times in free jet as compared to the present case due to high interaction area with the surrounding. Namgyal and Hall [23] also found a higher entrainment ratio as compared to the present case. This is due to the uniform jet exit profile and a higher jet exit Reynolds number, which increase the entrainment into the flow stream.

5.2.6 Reynolds stresses

The Reynolds stresses for configuration 1 and configuration 2 in the wall-normal direction are shown in Figure 5.25. The Reynolds stresses in wall-normal direction are calculated at the jet centerline plane. The Reynolds stresses and its locations in wall-normal direction are normalised with the square of the local maximum streamwise velocity $\left(u_{max}^2\right)$ and jet half-width $\left(y_{1/2}\right)$ respectively. From the Figure 5.25, it can be seen that the Reynolds stresses get affected by the sidewall very near the jet exit. In the upper shear layer, at the downstream location of $x/h = 5$, the Reynolds stress component $< u'v' >$ shows a higher value as compared to the other Reynolds stress components $< u'w' >$ and $< v'w' >$. But very close to the bottom wall, the Reynolds stress $< u'v' >$ shows the negative value. This is due to the higher wall-normal velocity fluctuation (v') as compared to the lateral velocity fluctuation (w'). The negative value of $< u'v' >$ close to the wall indicates the mixing and flow of the fluid in opposite direction. In the inner shear layer, at $x/h = 5$, both the configurations show similar variation of Reynolds stress whereas the deviation in Reynolds stresses is observed in the upper shear layer. The location of zero shear stress component $< u'v' >$ is lower than the y_{max} in configuration 1, while in configuration 2, due to the limitation of the lateral spread in configuration 2, the location of y_{max} comes closer to the zero shear stress $< u'v' >$ component. The configuration 2 shows the higher value of Reynolds stress component $< u'v' >$ as compared to configuration 1 due to the presence of sidewall. But the Reynolds stress component $< u'w' >$ shows higher value in configuration 1 as compared to configuration 2 due to the increase in the fluctuating component of w in configuration 1 as compared to configuration 2. This indicates that mixing is more prominent in configuration 1 as compared to configuration 2 in the vertical centerline plane. The difference of Reynolds stresses is more prominent where flow interacts with the sidewalls. Further downstream, $x/h = 15$, the jet spreads in all the three directions and flow-stream starts interacting with the sidewalls. This increases the fluctuation of velocity components but reduces the transverse velocity component (w). The fluctuation of velocity component enhances the Reynolds stresses in upper shear layer whereas

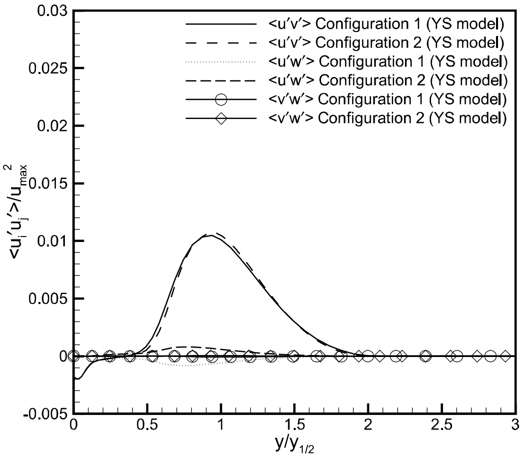

(a) $x/h = 5$

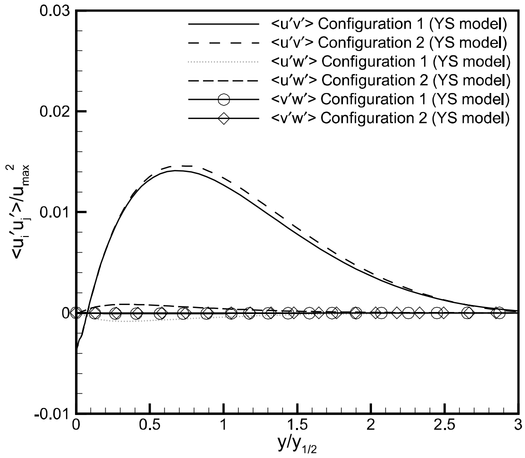

(b) $x/h = 15$

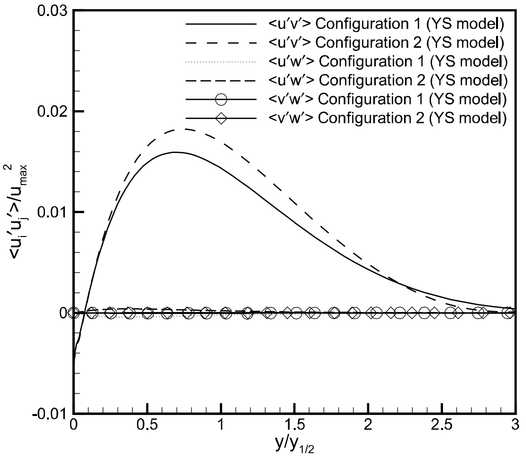

(c) $x/h = 30$

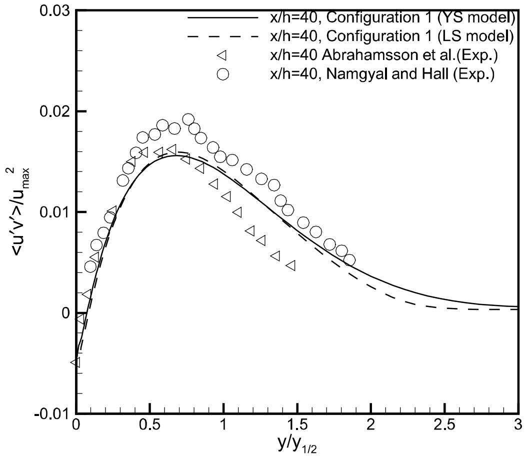

(d) $x/h = 40$

Figure 5.25: Reynolds shear stress in wall-normal direction at jet centerline plane

in the lower shear layer, it shows the similar variation in both the configurations. The Reynolds stress $< u'v' >$ is still dominating at this location as compared to $< u'w' >$ and $< v'w' >$. The Reynolds stress $< u'v' >$ in configuration 2 increases by about 10% as compared to configuration 1 at $x/h = 30$. The Reynolds stress component $< u'w' >$ shows a reversed trend in configuration 1 as compared to configuration 2 due to the formation of strong lateral velocity field. The Reynolds stress component $< v'w' >$ is very small in the whole domain due to the negligible velocity component w' in the vertical centerline plane. The Reynolds stresses in wall-normal direction are calculated using YS and LS turbulence models and compared in Figure 5.25d. Both the YS and LS models show similar behaviour of the Reynolds shear stress component$< u'v' >$ adjacent to the bottom wall in the inner shear layer, but near the y_{max}, the LS model predicts higher value of Reynolds stress component$< u'v' >$. This indicates that the mixing of the flow stream is higher in the LS model leading to a little higher decay of the maximum velocity (see section 5.2.1). In the outer shear layer $y/y_{1/2} > 1.4$, the YS model predicts higher value of $< u'v' >$ than the LS model. This leads to a higher diffusion and mixing of the fluid in the outer shear layer in the YS model. This behaviour of the model leads to a higher diffusion of the thermal energy resulting into a higher decay of temperature field predicted by YS model (see section 5.2.1). The normal variation of dominating Reynolds stress $< u'v' >$ is also compared with Abrahamsson et al. [12] and Namgyal and Hall [23] at $x/h = 40$ in Figure 5.25d for configuration 1. The numerically calculated Reynolds stress for the developing condition shows similar variation of Reynolds stress calculated experimentally by different authors at $x/h = 40$. The listed authors found a higher Reynolds stress as compared to the present case due to the different velocity profiles created by the nozzle geometry and jet exit Reynolds number.

The lateral variation of Reynolds shear stresses is shown in Figure 5.26. The Reynolds stresses in the lateral direction are calculated at the y_{max} plane across the jet. The Reynolds stresses and its location in lateral direction are normalised by square of the local maximum streamwise velocity $\left(u_{max}^2\right)$ and lateral jet half-width $(z_{1/2})$ respectively. From the Figure 5.26, it can be seen that the Reynolds shear stress in the lateral direction achieves a peak value near $z_{1/2}$. The Reynolds stress $< u'w' >$shows the dominance over the other Reynolds stress components $< u'v' >$ and $< v'w' >$. This is due to the increase in the lateral velocity component w. At $x/h = 5$, the Reynolds stress component $< u'v' >$ is small and positive but significantly larger than $< v'w' >$. This nature of Reynolds stress is obtained due to the spreading nature of the flow. Further downstream, i.e. $x/h = 15$ and 30, the Reynolds stress $< u'v' >$ is negative. This is because of the entrainment of fluid into the flow stream. In the configuration 1, the transverse velocity component is a little larger

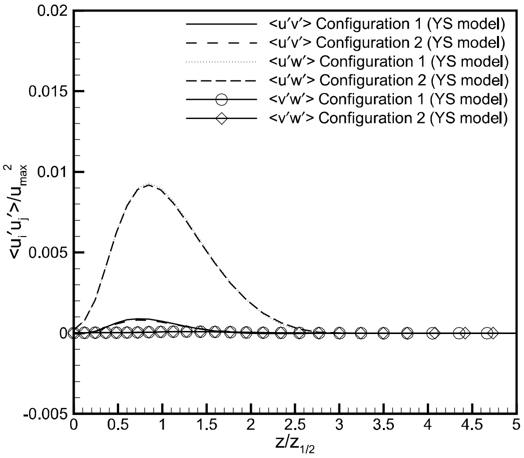

(a) $x/h = 5$

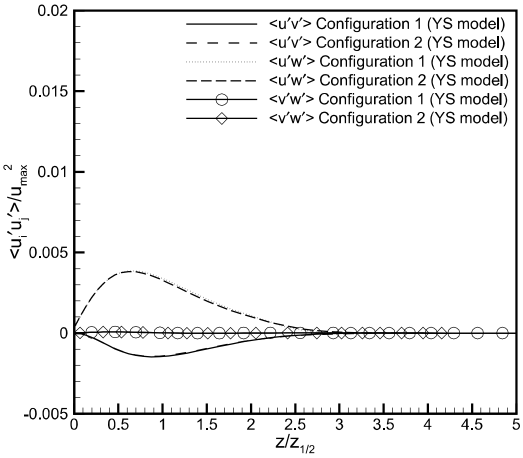

(b) $x/h = 15$

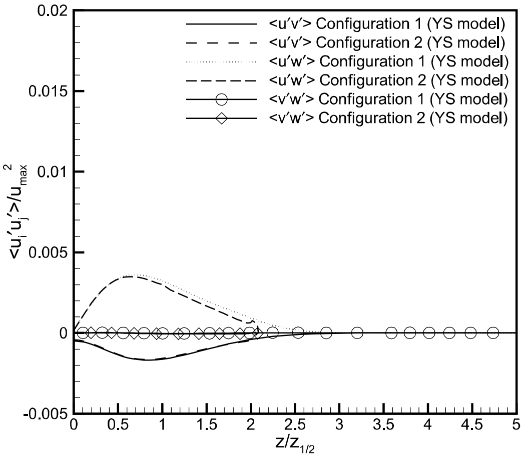

(c) $x/h = 30$

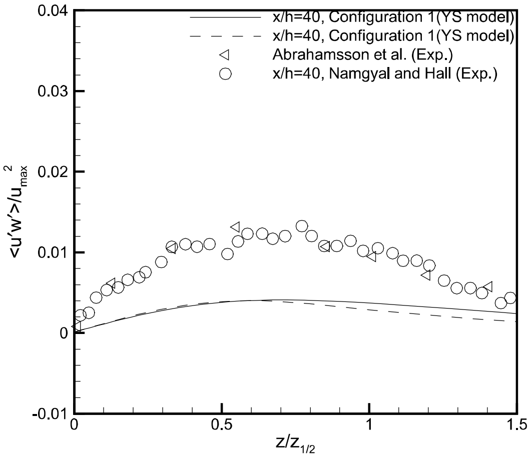

(d) $x/h = 40$

Figure 5.26: Reynolds shear stress $\left(< u'w' > / u^2_{max}\right)$ in lateral direction at y_{max} plane

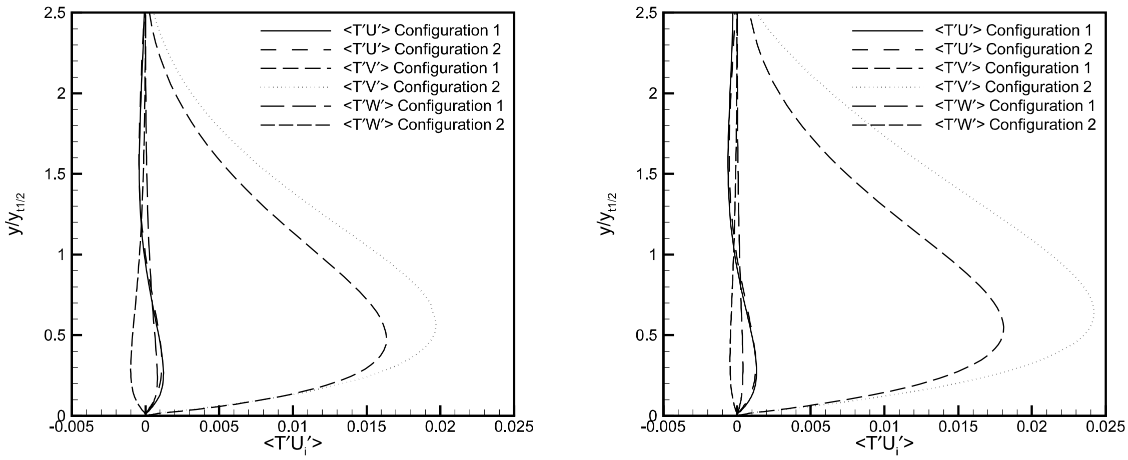

(a) (b)

Figure 5.27: Turbulent heat flux (YS model) variation in wall-normal direction at (a) $x/h = 15$ and (b) $x/h = 30$

than configuration 2. Due to this, configuration 1 shows a little higher Reynolds shear stress as compared to configuration 2. The Reynolds shear stress $< u'w' >$ is also compared with the results of Abrahamsson et al. [12] and Namgyal and Hall [23] at $x/h = 40$ in Figure 5.26d. Abrahamsson et al. [12] and Namgyal and Hall [23] utilized jet with the top hat initial velocity profile and higher Reynolds numbers, which resulted in a higher rate of mixing and turbulent structure with the ambient fluid. This leads to an increase in the Reynolds shear stress as compared to the present case.

5.2.7 Turbulent heat flux

The distribution of turbulent heat flux in the wall-normal direction for configuration 1 and configuration 2 is shown in Figure 5.27. The turbulent heat fluxes in the different directions are calculated as $< t'u_i' >= -(\nu_t/Pr_t)(dT/dx_i)$ and compared at the downstream locations x/h = 15 and 30. The calculated turbulent heat fluxes and their respective locations are normalised as $< T'U_i' >=< t'u_i' > /(t_c u_{max})$ and thermal half-width respectively. Where, t_c and u_{max} represent the local centerline mean temperature and maximum streamwise velocity respectively. The YS and LS models show almost a similar behaviour of the jet. So, here only YS model is shown for the brevity. The turbulent heat flux $< T'U' >$ indicates the turbulent heat transport in the downstream $(x - axis)$ direction due to the temperature and streamwise velocity fluctuations whereas $< T'V' >$ and $< T'W' >$ represent the turbulent heat transport in the wall-normal $(y - axis)$ and lateral

($z-axis$) directions respectively. In the vertical jet centerline plane, it can be seen that the lateral heat flux component $< T'W' >$ is comparatively low in both the configurations due to decrease in the temperature gradient dT/dz as compared to the temperature gradients dT/dx and dT/dy. The lateral heat flux $< T'W' >$ at $x/h = 15$ is marked positive for configuration 1 whereas in configuration 2, this trend gets reversed due to sidewalls. From the contour plot of w velocity component, it can be seen that in configuration 1, a higher velocity gradient is formed in the reverse direction. This leads to the opposite characteristic of lateral heat flux component in configuration 2 as compared to configuration 1 on the vertical jet centerline plane. The variation of streamwise heat flux $< T'U' >$ in the lower shear layer is positive in both the configurations. This indicates either $T' > 0$ and $U' > 0$ or $T' < 0$ and $U' < 0$. Due to cold surrounding in comparison to the heated jet and the spreading behaviour of the jet, the streamwise turbulent heat flux from the lower shear layer is transported in neighboring shear regions; so fluctuating quantities become $T' > 0$ and $U' > 0$. The value of streamwise heat flux $< T'U' >$ in the upper shear layer is less than zero. This indicates either $T' > 0$ and $U' < 0$ or $T' < 0$ and $U' > 0$. But here, due to heated jet, heat is transported from the lower shear region and entrainment takes place from the surrounding in upper shear layer so fluctuating quantities become $T' > 0$ and $U' < 0$ in the upper shear layer. The wall-normal heat flux component $< T'V' >$ is positive and higher than the other heat fluxes in the whole domain. The heat flux profile reveals that diffusion of thermal energy in wall-normal direction is dominated by the heat flux component $< T'V' >$. This is due to the presence of sidewalls in configuration 2. Due to sidewalls, the normal turbulent heat flux component $< T'V' >$ in configuration 2 increases approximately by 15% than in configuration 1. Similar behaviour is noticed at the downstream location $x/h = 30$ but the value is reduced a little bit. This happens because flow is developed at this location in both the configurations.

The distribution of turbulent heat flux in the lateral direction in configuration 1 and configuration 2 at the downstream locations $x/h = 15$ and 30 is shown in Figure 5.28. The lateral variation of heat flux is calculated at the y_{max} plane. The lateral variation of heat fluxes are positive except $< T'W' >$ at the downstream locations $x/h = 15$ and 30. From the contour plot of u and v velocity components, it can be seen that u and v velocity components show the spreading behaviour of the flow in the lateral shear layer. This behaviour of turbulent heat fluxes reveals that heat is transported outside from the shear layers due to $< T'U' >$ and $< T'V' >$. The $< T'W' >$ heat flux component is responsible for the heat transport between the different shear layers.

The results from both the YS and LS models are compared at the downstream location $x/h = 40$ for the lateral and wall-normal directions as shown in Figure 5.29. From the

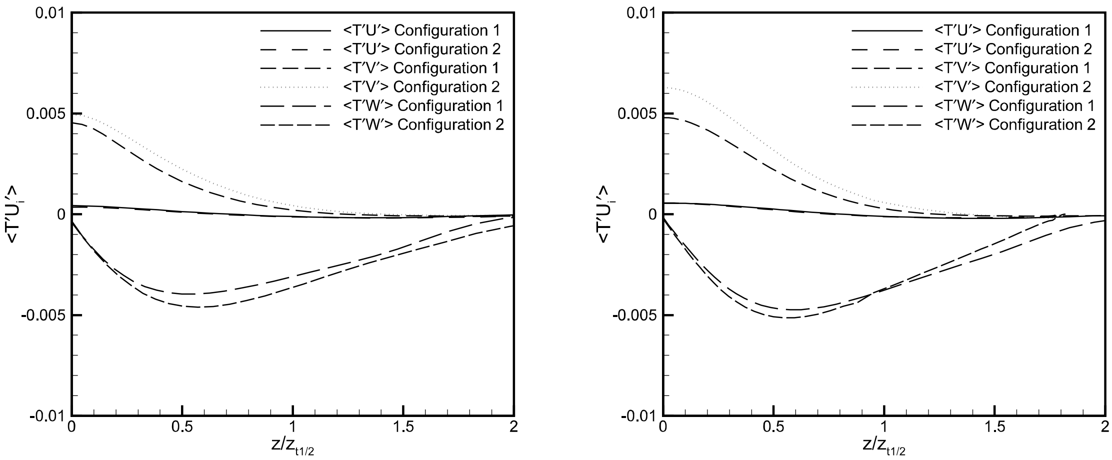

(a) (b)

Figure 5.28: Turbulent heat flux (YS model) variation in lateral direction at (a) $x/h = 15$ and (b) $x/h = 30$

Figure 5.29, it can be seen that the LS model predicts higher value of turbulent heat flux in the wall-normal and lateral directions than the YS model. This is due to the generation of higher Reynolds stresses by LS model (near the y_{max} in upper shear layer, see section 5.2.6) than the YS model resulting into a higher turbulent viscosity (ν_t) in the LS model.

5.3 Conclusion

The effect of jet exit temperature $\left(t_{jet} = 20^0C, 40^0C\right)$ and sidewall effect on the heat transfer and mean flow characteristics is characterised by the experimental methods. The temperature and mean velocity field are used for the validation of the numerical methods. The turbulent flow characteristics of the sidewall conditions are discussed through numerical method. For this, two different sidewall configurations have been considered, i.e. configuration 1 (without sidewall) and configuration 2 (with sidewall). Based on the present results the following conclusions can be drawn through experimental and numerical methods:

- The measured heat transfer characteristics of the wall jet in configuration 1 and configuration 2 is characterized as: The bottom wall temperature decay is higher for configuration 1 as compared to configuration 2 due to the presence of sidewall. The lateral surface temperature variation shows the similar pattern for both the configurations in most of the regions, before the attachment of the flow stream to the side-

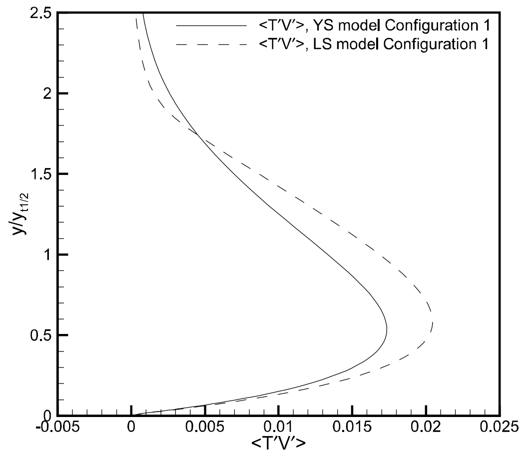

(a)

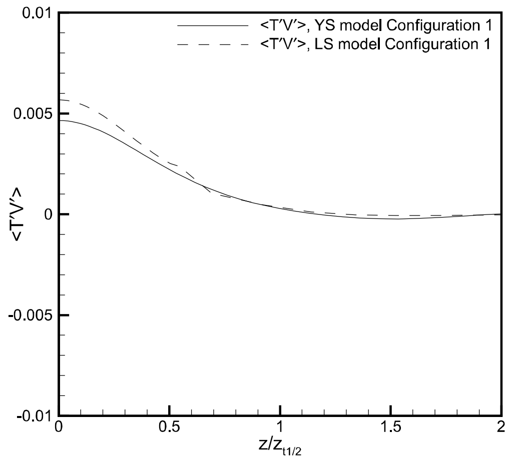

(b)

Figure 5.29: Turbulent heat flux comparison for YS and LS turbulence models in configuration 1 at $x/h = 40$ (a) wall-normal direction (b) lateral direction

wall in configuration 2. But, on the edge in the lateral directions, the temperature gradually increases due to the accumulation of the turbulent ripple in configuration 2. The variation of jet centerline temperature shows the similar pattern as the bottom wall temperature decay. It is found that the rate of thermal spread of the jet in wall-normal direction is higher in configuration 2 as compared to configuration 1, due to the restriction of spread in the lateral direction. The configuration 2 shows the early thermal stability as compared to configuration 1 due to the less interaction and mixing of the ambient fluid. The thermal turbulent fluctuation has been studied with the help of K-type thermocouple. The minimum fluctuation is observed at the jet centerline due to less production of the turbulent eddies. This fluctuation is found to gradually increase in the lateral direction due to entrainment of the ambient fluid into the flow stream. It shows the maximum fluctuation near the interface. The configuration 1 and the configuration 2 show the similar pattern of the thermal fluctuation along the jet centerline, but the range of fluctuation is decreased in configuration 2 due to the uniformity of the temperature. A statistical analysis is also done on the basis of the single point temperature fluctuation. The probability density function (PDF) shows the normal distribution for configuration 1. However, the normal distribution is lost for configuration 2 at $x/h = 20$ due to the interaction of the flow stream with the sidewall. Further in downstream directions, again both the configurations show the similar pattern adhering to the normal distribution curve.

The skewness and flatness factors are close to the Gaussian value in most of the regions. The skewness factor in the near field is negative for both the configurations due to the dominance of convection from the hot jet stream. And, this negative skewness stays longer for configuration 2 as compared to configuration 1.

- Based on the numerical results, the following conclusions are drawn: The decay rate of centerline temperature in configuration 1 is $\sim 25\%$ higher than in configuration 2, whereas the decay rate of maximum streamwise velocity in configuration 1 is decreased by about $\sim 8-9\%$ as compared to configuration 2. The LS model shows higher accuracy for predicting the decay rate for the velocity field, whereas YS model shows higher accuracy for predicting the temperature field. The contour plots of YS and LS turbulence models suggest that the velocity spread in configuration 1 is higher as compared to configuration 2, which resulted in a higher spread of the temperature field in configuration 1 than in configuration 2. Initially, the turbulent kinetic energy in configuration 1 is higher as compared to configuration 2, but in the downstream locations, due to the sidewall interaction with the flow stream, the generation of maximum turbulent kinetic energy in configuration 2 is increased by nearly 10% as compared to that in configuration 1. The entrainment of the ambient fluid in configuration 1 is higher as compared to configuration 2 due to the higher area of interaction with the surrounding fluid. The Reynolds stresses in both the configurations show the spatial variation. The Reynolds shear stress $< u'v' >$ dominates in the vertical jet centerline plane whereas $< u'w' >$ dominates in lateral direction at the y_{max} plane in both the configurations. The Reynolds shear stress $< u'v' >$ is increased by nearly 10% in configuration 2 as compared to configuration 1. The location of zero shear stress component $< u'v' >$ is lower than the y_{max} in configuration 1, while in configuration 2, the location of y_{max} comes closer to the zero shear stress $< u'v' >$ component. The turbulent heat flux $< T'V' >$ dominates in the lateral and wall-normal shear layers in both the configurations. The turbulent heat flux $< T'V' >$ increases by approximately 15% due to the sidewall interaction in configuration 2.